Journal Pre-proof

A multi-domain model for microcirculation in optic nerve: Blood flow and oxygen transport

Zilong Song, Shixin Xu, Robert Eisenberg, Huaxiong Huang

PII: S0167-2789(24)00223-9
DOI: https://doi.org/10.1016/j.physd.2024.134272
Reference: PHYSD 134272

To appear in: *Physica D*

Received date : 20 January 2024
Revised date : 9 April 2024
Accepted date : 17 June 2024

Please cite this article as: Z. Song, S. Xu, R. Eisenberg et al., A multi-domain model for microcirculation in optic nerve: Blood flow and oxygen transport, *Physica D* (2024), doi: https://doi.org/10.1016/j.physd.2024.134272.

A multi-domain model for microcirculation in optic nerve: blood flow and oxygen transport

Zilong Song[a], Shixin Xu[b], Robert Eisenberg[c,d], Huaxiong Huang[e,f,g]

[a]*Department of Mathematics and Statistics, Utah State University,3900 Old Main Hill,Logan,84322, UT,USA*
[b]*Duke Kunshan University, 8 Duke Ave, Kunshan, Jiangsu, China*
[c]*Department of Applied Mathematics, Illinois Institute of Technology, Chicago, 60616, IL, USA*
[d]*Department of Physiology and Biophysics, Rush University, Chicago, 60612, IL, USA*
[e]*Research Centre for Mathematics, Advanced Institute of Natural Sciences, Beijing Normal University (Zhuhai), China*
[f]*BNU-HKBU United International College, Zhuhai China*
[g]*Department of Mathematics and Statistics, York University, Toronto, M3J 1P3, ON, Canada*

Abstract

Microcirculation of blood and transport of oxygen play important roles in the biological function of the optic nerve and its diseases. This work develops a multi-domain model for the optic nerve, that includes important biological structures and various physical mechanisms in blood flow and oxygen delivery. The two vascular networks are treated as five domains in the same geometric region, with various exchanges among them (such as Darcy's law for fluid flow) and with the tissue domain (such as water leak, diffusion). The numerical results of the coupled model for a uniform case of vasculature distribution show mechanisms and scales consistent with literature and intuition. The effects of various important model parameters (relevant to pathological conditions) are investigated to provide insights into the possible implications. The vasculature distribution (resting volume fractions here) has significant impacts on the blood circulation and could lead to insufficient blood supply in certain local regions and thereby affect the delivery of oxygen. The water leak across the capillary wall will have nontrivial effects after the leak coefficients pass a threshold. The pulsatile arterial pressure leads to expected pulsatile patterns and stable spatial profiles, and the uniform case is almost the averaged version of pulsatile case. The effects of viscosity, the stiffness of blood vessel wall, oxygen demand, etc. have also been analyzed.

The framework can be extended to include ionic transport or to study the retina when more biological structural information is available.

Keywords: microcirculation, optic nerve, oxygen transport, blood flow, multi-domain model

1. Introduction

Most of biology involves complex structures that are nearly machines designed to perform biological functions. Machines in our technology cannot be understood without their structure as well as the physics that they use and the engineering function they perform. A natural approach for these biological problems is to use physical laws in the form of conservation laws in three dimensions and time, together with structural information presented by biologists, and to compute physiological results required by biologists and clinicians. This approach has been used to study biological systems of some complexity, for example, the electrocytes of electrical eels [1, 2], the optic nerve of amphibians [3], and the lens of the eye [4]. The history of this approach is reviewed in [5].

The eye is made of a series of tissue structures such as the lens, the retina, and the optic nerve that work together. The retina converts the light to electric signals, which travel to the brain through the optic nerve. In each tissue structure, many physical mechanisms [6, 7, 8] involving fluid flow and transport of ions and oxygen work together in well-designed biological structures to achieve specific goals and maintain homeostasis. Many eye diseases such as glaucoma [9] and diabetic retinopathy [10, 11] are due to the damage of the optic nerve and retina related to the coupling of the above mechanisms. Cardiovascular pathologies such as hypertension and diabetes can induce changes in microcirculation in the retina and optic nerve, and then are reflected by functional or structural changes. Non-invasive experimental/clinic data from the eye (say the retina) can provide an important "window" into the cardiovascular pathologies [12, 13]. Therefore, mathematical modeling is needed to uncover the relationship between diseases/alterations in structures and the physical mechanisms. The challenges are the coupling of different mechanisms in multiple time and spatial scales as well as the incorporation of crucial biological structural information. On the other hand, too many scales and too much cellular detail in the model will make analysis/computation extremely tricky.

There have been many modeling and experimental studies [6, 14, 15, 16, 17] for both the retina and the optic nerve, particularly for the retina since vascular and geometrical information is more accessible experimentally. The book [6] includes an excellent review of different levels of mathematical models for blood flow in the eye as well as oxygen transport, see also [18, 19, 20, 7]. The microcirculation and autoregulation have been studied in [21, 22, 16, 23, 24]. A recent work [25] has studied the coupling between the blood microcirculation and oxygen transport in retina, where a computer-generated vascular tree network is used for blood flow in vessels and delivery of oxygen to the tissue. A one-dimensional model of blood circulation in retina arterial network has been developed by utilizing clinic imaging [26]. A viscoelastic and porous-media model [27, 15] has been developed to study the mechanics and hemodynamics of the optic nerve head. The blood flow and neurovascular coupling mechanisms in the optic nerve have been reviewed in [28].

Multi-domain modeling has shown success in the study of complex biological tissues, such as the lens [4], the optic nerve [3, 29], brain tissue [30], and cardiac tissue [31, 32]. At the tissue (coarse-grained) level, a given spatial point is present in every domain in the multidomain model, where exchanges occur between domains (to represent mechanisms at a refined cellular level). In particular, a tridomain model [3, 29] has been developed for fluid flow and electrodiffusion in the optic nerve (without vasculature), and the clearance of potassium is studied. The multi-domain model for the vasculature here can be treated as a generalization of the compartment (vessel segment) models [33, 6], in the sense that more spatial and structural information could be incorporated.

The objective of this work is to develop a multi-domain model for blood microcirculation and oxygen transport in the optic nerve, with important biological structures and physical mechanisms incorporated. This work will focus on the vasculature and the exchanges between the vasculature and tissue in the optic nerve, and can potentially be combined with the previous tri-domain model on fluid flow and electrodiffusion of ions in tissue [3, 29] in future work. This work studies the optic nerve because of its relatively simple geometric structure, but the framework can be generalized to the retina. The multi-domain model has six domains, including five vascular domains (two sets of artery-capillary pairs that share a common venous tree) and one extravascular domain. To model blood circulation, we utilize Darcy's law for in-domain flow and also include the leak to the tissue (the changes are

related to the diseased state) and changes of volume fraction (equivalently blood vessel radius) due to force balance. The oxygen transport considers both the dissolved and bound oxygen in hemoglobin and incorporate the mechanisms due to diffusion, convection, and oxygen consumption.

The coupled model is solved by a finite-difference scheme and a Matlab solver (ode15s). The simulated results for the baseline case with a uniform resting volume fraction show reasonable mechanisms and consistent scales for important quantities with literature. More importantly, the effects of non-uniform resting volume fractions, pulsatile boundary conditions, and various parameters are studied to provide insights into the consequences of biological structural changes and parameter changes due to diseases. For example, with a non-uniform distribution of resting volume fractions, local regions could suffer insufficient capillary exchanges and oxygen supply. The leak coefficient could have strong impact on blood circulation and oxygen delivery after it passes a threshold. With pulsatile boundary arterial pressures, the results show almost the same averaged quantities over one period as the baseline simulation with constant pressure conditions. The effects of viscosity, the stiffness of the blood vessel wall, the demand for oxygen, the local partial blockage of vasculature, etc. have also been analyzed.

The manuscript is organized as follows. Section 2 develops the mathematical model of blood circulation and oxygen transport with six domains. The model is simulated in Section 3 for a baseline case with uniform resting volume fractions and constant boundary pressures. In Section 4, we investigate the effects and sensitivity of physical parameters including leak coefficients, blood viscosity, modulus of the blood vessel wall, the permeability of blood flow, oxygen consumption parameters, boundary arterial pressure and boundary oxygen supply parameters. The effects of biological structural changes are also analyzed in Section 4, through changes of resting (nonuniform) volume fractions. Conclusions are provided in Section 5.

2. A Hexa-Domain Model

Some abbreviations are listed in Table 1 for easy reading. Figure 1(a) sketches the optic nerve, where the retrolaminar region is the major region with nearly radial symmetry. In this work, we focus on the retrolaminar region in the optic nerve [15, 6, 34, 35]. We consider six overlapping domains for the vasculature and tissue in the same geometric domain $\Omega = \{(r, z)|R_0 < r < R_1, 0 < z < L\}$ in cylindrical coordinates as shown in Figure 1(a). It

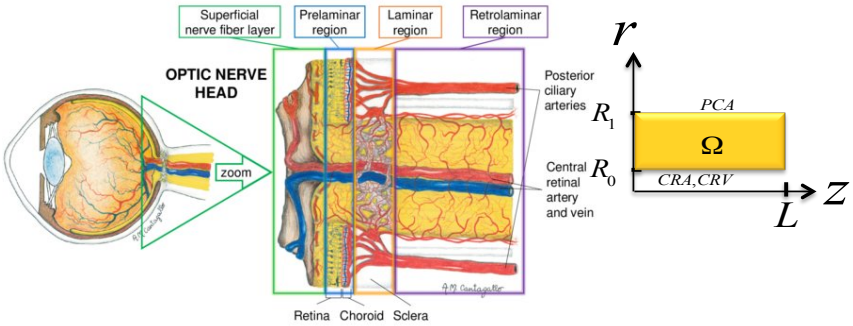

(a) Optic nerve and domain Ω

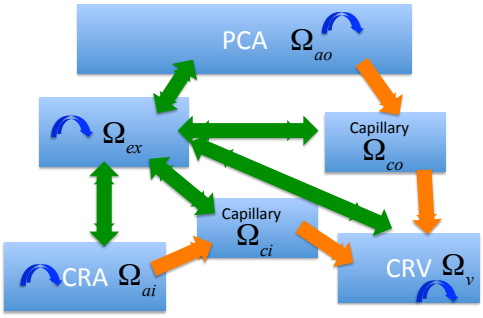

(b) Six domains and pathways

Figure 1: (a) The optic nerve and retrolaminar region in an axial sectional view. The left figure is taken from [28] with permission.The right figure sketches the geometric domain Ω considered in this work. (b) Six domains including 5 vascular and one extravascular domains. The green arrows denote the water exchanges between the vascular domain and tissue (extra-vascular domain), the orange arrows denote the blood flow pathways, and the blue arrows denote the in-domain blood circulation.

CRA	Central Retinal Artery	CRV	Central Retinal Vein
PCA	Posterior Ciliary Artery	RBC	Red Blood Cell
MAP	Mean Arterial Pressure	1D	one-dimensional

Table 1: Abbreviations in the paper

is assumed to be uniform (or averaged) in the longitudinal z direction so that the model considered in this paper is one-dimensional (1D) in the radial direction and symmetric about $r = 0$. The six domains are sketched in Figure 1(b) and are defined as:

Ω_{ai}: Arteries and arterioles starting from CRA at inner boundary $r = R_0$

Ω_{ao}: Arteries and arterioles starting from PCA at outer boundary $r = R_1$

Ω_v: Veins and venules connected to CRV at $r = R_0$

Ω_{ci}: Capillaries between Ω_{ai} and Ω_v

Ω_{co}: Capillaries between Ω_{ao} and Ω_v

Ω_{ex}: the extra-vascular domain, i.e, tissue domain including the axons and glial cells and extracellular space.

In the above, each of the domains Ω_j $(j = ai, ao, v, ci, co, ex)$ occupies the same geometric domain Ω in Figure 1(a), the first five are the vascular domains for the two sets of vasculature networks and the last one is the tissue or extra-vascular domain.

2.1. Water/blood circulation

The water/blood circulation in the optic nerve is based on porous-media type flows and exchanges among the domains. The circulation is both the blood flow among the vascular domains (the first 5 domains above) and the water flow (leak) for the exchange between vascular and extravascular domains. For the 1D geometric region $R_0 < r < R_1$, the governing equations

from conservation laws are

$$\begin{aligned}
&\frac{\partial \eta_{ai}}{\partial t} + \frac{1}{r}\frac{\partial \left(r\eta_{ai}u_{ai}^{r}\right)}{\partial r} + Q_{ai,ex} + Q_{ai,ci} = 0,\\
&\frac{\partial \eta_{ao}}{\partial t} + \frac{1}{r}\frac{\partial \left(r\eta_{ao}u_{ao}^{r}\right)}{\partial r} + Q_{ao,ex} + Q_{ao,co} = 0,\\
&\frac{\partial \eta_{v}}{\partial t} + \frac{1}{r}\frac{\partial \left(r\eta_{v}u_{v}^{r}\right)}{\partial r} + Q_{v,ex} + Q_{v,co} + Q_{v,ci} = 0,\\
&\frac{\partial \eta_{ci}}{\partial t} + Q_{ci,ex} - Q_{ai,ci} - Q_{v,ci} = 0,\\
&\frac{\partial \eta_{co}}{\partial t} + Q_{co,ex} - Q_{ao,co} - Q_{v,co} = 0,\\
&\frac{1}{r}\frac{\partial}{\partial r}\left(\sum_{k=ai,ao,v,ex}\eta_{k} r u_{k}^{r}\right) = 0,\\
&\eta_{ai} + \eta_{ao} + \eta_{v} + \eta_{ex} + \eta_{ci} + \eta_{co} = 1,
\end{aligned} \tag{1}$$

where η_j is the volume fraction of each domain Ω_j $(j = ai, ao, v, ci, co, ex)$, the spatial derivative terms $\frac{1}{r}\frac{\partial}{\partial r}\left(r(\eta_k u_k^r)\right)$ are the in-domain flows in the polar coordinates with velocity u_k^r $(k = ai, ao, v, ex)$, all the $Q_{i,j}$ are the exchanges between different domains. There are in-domain flows in artery and vein domains, since they are connected with branching structures. There is also in-domain flow in the extravascular domain since it is spatially connected. But there are no in-domain flows for capillary domains at this tissue-scale modeling, because they are only connected to arteries and veins at a smaller spatial scale and different capillary networks do not exchange directly with each other. The second to last equation is derived by combining the dynamics of η_{ex} and the algebraic constraint in the last equation. We will present the detailed models for all the terms in the above equation and boundary conditions in the next subsections.

2.1.1. In-domain flows and permeability

The in-domain velocity in vascular domains follows the Darcy's law

$$u_k^r = -\frac{\kappa_k(r)\tau_k}{\mu_b}\frac{\partial p_k}{\partial r}, \quad k = ai, ao, v, \tag{2}$$

where κ_k is the in-domain blood permeability, μ_b is the viscosity of blood, and τ_k is the tortuosity. The tortuosity τ_k includes the effect of vessel structure and orientation of blood vessels (in r-direction). From derivations in

Appendix A.1 and [15], the permeability is given by

$$\kappa_k(r) = \frac{1}{8}\beta_k(r)\eta_k, \quad k = ai, ao, v, \tag{3}$$

where $\beta_k(r)$ depends on the structure of blood vessels, e.g., the distribution of branches, the level of branching, segment length, etc. But for simplicity, the coefficient $\beta_k(r)$ is assumed to be a constant here, and its value is estimated in the Appendix A.1. The permeability κ_k may depend on the concentration of oxygen through the changes in η_k due to changes in the vessel wall properties. For the extravascular domain Ω_{ex}, we set

$$u_{ex}^r = -\frac{\kappa_{ex}\tau_{ex}}{\mu_{ex}}\frac{\partial p_{ex}}{\partial r}, \tag{4}$$

where $k_{ex}, \tau_{ex}, \mu_{ex}$ are the permeability, tortuosity and viscosity in Ω_{ex}.

2.1.2. Exchange through blood vessel wall

Here, we consider the water exchange rates $Q_{j,ex}$ between the vascular domains Ω_j $(j = ai, ao, v, ci, co)$ and the extravascular domain Ω_{ex}, due the leak/exchange through the blood vessel wall. The water exchange rate $Q_{j,ex}$ per unit control volume follows the form

$$Q_{j,ex} = M_{j,ex}U_{j,ex}, \quad j = ai, ao, v, ci, co, \tag{5}$$

where $M_{j,ex}$ is the area of blood vessel wall for domain Ω_j per unit control volume and $U_{j,ex}$ is the water velocity from Ω_j to Ω_{ex}. The quantity $M_{j,ex}$ is modeled by (see Appendix A.1 for details)

$$M_{j,ex} = M_{j,ex}^0\sqrt{\eta_j}, \tag{6}$$

where $M_{j,ex}^0$ is a constant depending on blood vessel structures and estimated in Appendix A.1 (related to β_j). The dependence of $M_{j,ex}$ on the radius of the blood vessel is reflected through η_j. The water velocity across the blood vessel wall is modeled as

$$U_{j,ex} = L_{j,ex}(p_j - p_{ex} - (\pi_j - \pi_{ex})), \quad j = ai, ao, v, ci, co \tag{7}$$

where $L_{j,ex}$ is the leak coefficient [36, 16] (for capillary, see also [37] [38] [39]), and π_j, π_{ex} are the colloidal osmotic pressures [16] (e.g., due to ions, proteins etc.). The leak coefficient in artery and vein domains is much smaller than that in capillary domains under normal conditions.

2.1.3. Exchange between vascular domains

The blood flow rates between the capillary domains and the connected artery or vein domain are modeled by

$$\begin{aligned} Q_{ai,ci} &= K_{ai,ci}(p_{ai} - p_{ci}), \quad Q_{v,ci} = K_{v,ci}(p_v - p_{ci}), \\ Q_{ao,co} &= K_{ao,co}(p_{ao} - p_{co}), \quad Q_{v,co} = K_{v,co}(p_v - p_{co}), \end{aligned} \tag{8}$$

where $K_{j,k}$ is the effective conductance (or the inverse of resistance). We take $K_{ai,ci}$ from artery domain Ω_{ai} to capillary domain Ω_{ci} for example. It relates to the conductance in both artery and capillary domains since it flows in the small arterioles for some distance before reaching the capillary. The conductance is modeled as the harmonic average

$$K_{ai,ci} = \frac{K_{ai}K_{ci}}{K_{ai} + K_{ci}}, \quad K_{ai} = \delta_{ai}\eta_{ai}^2 \frac{\epsilon_{ai}}{\tanh(\epsilon_{ai})}, \quad K_{ci} = \delta_{ci}\eta_{ci}^2 \frac{\epsilon_{ci}}{\tanh(\epsilon_{ci})}, \tag{9}$$

where K_j $(j = ai, ci)$ is the effective conductance in Ω_j with parameter δ_j estimated in Appendix A.1 (related to β_j and μ_b). The dimensionless ratio $\epsilon_j/\tanh(\epsilon_j)$ (with $j = ai, ci$) is a correction factor due to the water leak [16]

$$\epsilon_j = \frac{1}{2}\sqrt{(M_{j,ex}L_{j,ex})/(\delta_j\eta_j^2)}, \quad j = ai, ci. \tag{10}$$

In the limit when there is no water leak through the blood vessel wall $L_{j,ex} \to 0$, we get $\epsilon_{ai} \to 0$ and $\epsilon_j/\tanh(\epsilon_j) \to 1$, so the correction factor has no effect. The presence of leak increases the conductance. In a similar way, we can define $K_{ao,co}$ $K_{v,ci}$, $K_{v,co}$, as well as the parameters δ_j, ϵ_j $(j = ao, co, v)$.

2.1.4. Force balance on blood vessel wall

The force balance on the blood vessel wall of each vascular domain is modeled by [16, 3]

$$\lambda_j(\eta_j - \eta_j^{re}) = p_j - p_{ex} - (P_j^{re} - P_{ex}^{re}), \quad j = ai, ao, v, ci, co, \tag{11}$$

where λ_j is the elastic modulus of the blood vessel wall [15, 40], P_j^{re}, P_{ex}^{re} are resting or reference pressures, and η_j^{re} is the resting volume fraction. The modulus λ_j is set as constant here, but it could be affected by the oxygen concentration and in turn leads to changes in volume fractions (or the radius of blood vessels). The quantity $\eta_j^{re}(r)$ could depend on the spatial variable r and the profile is related to the structural information. We investigate both uniform and Gaussian profiles for $\eta_j^{re}(r)$ in the simulations.

Remark 1: An alternative model of force balance [26, 41] uses $\sqrt{\eta_j}$ and $\sqrt{\eta_j^{re}}$ in the formula (11). If η_j is not far from η_j^{re}, the two models will be similar up to first-order approximations with slightly different definitions for the modulus.

2.1.5. Boundary conditions

As there are in-domain flows (i.e., spatial derivatives) for the four domains Ω_j $(j = ai, ao, v, ex)$, we need to propose boundary conditions at $r = R_0, R_1$ for these domains.

(1) For the artery domain Ω_{ai}, we set

$$p_{ai}(R_0, t) = P_{ai,0}(t), \quad \frac{\partial p_{ai}}{\partial r}(R_1, t) = 0, \tag{12}$$

where $P_{ai,0}$ is the given CRA pressure at the start of that artery domain Ω_{ai}. The condition at the outer boundary $r = R_1$ means no blood flow out of the domain there. Alternatively, if $P_{ai,0}(t)$ is not given, we can use the prescribed blood flow rates at the boundary

$$\eta_{ai} R_0 u_{ai}^r = Q_{ai}^*. \tag{13}$$

(2) For the other artery domain Ω_{ao}, we set

$$\frac{\partial p_{ao}}{\partial r}(R_0, t) = 0, \quad p_{ao}(R_1, t) = P_{ao,1}(t), \tag{14}$$

where $P_{ao,1}$ is the given PCA pressure at the start of artery domain Ω_{ao} and there is no blood flow on the inner boundary. Alternatively, if $P_{ao,1}(t)$ is not given, we can use the flow rates condition

$$\eta_{ao} R_1 u_{ao}^r = -Q_{ao}^*. \tag{15}$$

(3) For the vein domain Ω_v, we set

$$p_v(R_0, t) = P_{v,0}(t), \quad \frac{\partial p_v}{\partial r}(R_1, t) = 0. \tag{16}$$

where $P_{v,0}(t)$ is the given CRV pressure at inner boundary where the blood drains out of this optic nerve region.

(4) For the extravascular domain Ω_{ex}, we set

$$\frac{\partial p_{ex}}{\partial r}(R_0, t) = 0, \quad \frac{\partial p_{ex}}{\partial r}(R_1, t) = 0, \tag{17}$$

which means no water flow out of the region through domain Ω_{ex}.

2.2. Oxygen transport

We start by introducing some background knowledge and notations. The total oxygen concentration $\bar{C}_{O_2}$ (per unit blood volume) in vascular domains consists of two parts: the dissolved oxygen and the oxygen bound to hemoglobin in red blood cells (RBC) [6, 19, 42]. Mathematically, we have

$$\bar{C}_{O_2} = C_{O_2} + H\, S_{O_2} \tag{18}$$

where C_{O_2} the dissolved oxygen, H is the oxygen-binding capacity of blood (per unit blood volume), and S_{O_2} is the oxygen saturation of Hemoglobin. In many works [7, 25], the dissolved oxygen concentration is often represented by oxygen partial pressure P_{O_2} with the formula

$$C_{O_2} = \alpha_{O_2} P_{O_2} \tag{19}$$

where α_{O_2} is the solubility coefficient of oxygen in blood. But in order to distinguish the pressure p_k for water/blood flows and the above oxygen partial pressure in domain Ω_k, we will directly use the oxygen concentration C_{O_2} in our model. The oxygen saturation S_{O_2} is given by Hill's equation [25, 19]

$$S_{O_2} = \frac{P_{O_2}^n}{P_{O_2}^n + P_{50}^n} = \frac{C_{O_2}^n}{C_{O_2}^n + C_{50}^n} \tag{20}$$

where we have multiplied α_{O_2} before P_{O_2} and P_{50} to get the last equality, $C_{50} = \alpha_{O_2} P_{50}$ is the half-saturation constant, and n is the Hill's exponent parameter. The quantity H is often written as [7]

$$H = [Hb] C_{Hb}, \tag{21}$$

where $[Hb]$ is the hemoglobin concentration per unit volume of blood and C_{Hb} is the oxygen-binding capacity of hemoglobin. Under normal conditions, the quantities $H, [Hb], C_{Hb}$ can be assumed as constants, see Table A.9 in Appendix A.2. But here we will also consider abnormal cases with large water leak through blood vessels, so the hemoglobin concentration and hence the quantity H can vary spatially, since hemoglobin can not leak out with water.

In each of the five vascular domains, we have the above quantities and relations. To simplify the notations, we will omit the subscript O_2 but add the domain subscript. In summary, we have

$$\bar{C}_k(C_k, H_k) = C_k + H_k \frac{C_k^n}{C_k^n + C_{50}^n}, \quad k = ai, ao, v, ci, co, \tag{22}$$

where $\bar{C}_k$, C_k and H_k are the total oxygen concentration, dissolved oxygen concentration, and oxygen-binding capacity of blood in the domain Ω_k. For the extravascular domain Ω_{ex}, only the dissolved oxygen concentration $C_{ex}(r,t)$ is needed and well-defined.

By conservation laws, the dynamics of H_k $(k = ai, ao, v, ci, co)$ are given by

$$\begin{aligned}
&\frac{\partial(\eta_{ai}H_{ai})}{\partial t} - \frac{1}{r}\frac{\partial}{\partial r}\left(r\eta_{ai}u_{ai}^{r}H_{ai}\right) + Q_{ai,ci}H_{ai} = 0,\\
&\frac{\partial(\eta_{ao}H_{ao})}{\partial t} - \frac{1}{r}\frac{\partial}{\partial r}\left(r\eta_{ao}u_{ao}^{r}H_{ao}\right) + Q_{ao,co}H_{ao} = 0,\\
&\frac{\partial(\eta_{v}H_{v})}{\partial t} - \frac{1}{r}\frac{\partial}{\partial r}\left(r\eta_{v}u_{v}^{r}H_{v}\right) + Q_{v,ci}H_{ci} + Q_{v,co}H_{co} = 0,\\
&\frac{\partial(\eta_{ci}H_{ci})}{\partial t} - Q_{ai,ci}H_{ai} - Q_{v,ci}H_{ci} = 0,\\
&\frac{\partial(\eta_{co}H_{co})}{\partial t} - Q_{ao,co}H_{ao} - Q_{v,co}H_{co} = 0,
\end{aligned} \tag{23}$$

Under normal conditions when all the water leak terms $Q_{j,ex}$ $(j = ai, ao, v, ci, co)$ through blood vessel walls are negligibly small compared with other terms $Q_{i,j}$ in blood flow equations in (1), this system is equivalent to the first five equations in (1) with constant solutions $H_k = H_0$ $(k = ai, ao, v, ci, co)$ (verified in simulations). Next, the equations for oxygen exchange are given by

$$\begin{aligned}
&\frac{\partial}{\partial t}(\eta_{ai}\bar{C}_{ai}) + \frac{1}{r}\frac{\partial\left(\eta_{ai}rJ_{ai}^{r}\right)}{\partial r} + S_{ai,ex} + S_{ai,ci} = 0,\\
&\frac{\partial}{\partial t}(\eta_{ao}\bar{C}_{ao}) + \frac{1}{r}\frac{\partial\left(\eta_{ao}rJ_{ao}^{r}\right)}{\partial r} + S_{ao,ex} + S_{ao,co} = 0,\\
&\frac{\partial}{\partial t}(\eta_{v}\bar{C}_{v}) + \frac{1}{r}\frac{\partial\left(\eta_{v}rJ_{v}^{r}\right)}{\partial r} + S_{v,ex} + S_{v,ci} + S_{v,co} = 0,\\
&\frac{\partial}{\partial t}(\eta_{ci}\bar{C}_{ci}) + S_{ci,ex} - S_{ai,ci} - S_{v,ci} = 0,\\
&\frac{\partial}{\partial t}(\eta_{co}\bar{C}_{co}) + S_{co,ex} - S_{ao,co} - S_{v,co} = 0,\\
&\frac{\partial}{\partial t}(\eta_{ex}C_{ex}) + \frac{1}{r}\frac{\partial\left(\eta_{ex}rJ_{ex}^{r}\right)}{\partial r} + S_{ex} - \sum_{j=ai,ao,v,ci,co} S_{j,ex} = 0,
\end{aligned} \tag{24}$$

where J_j^r $(j = ai, ao, v, ex)$ are the in-domain oxygen fluxes in the r-direction, $S_{i,j}$ are the oxygen exchange rates between different domains, and S_{ex} is the consumption rate of oxygen (e.g., for pumps of ions in axons [8]) given by

the classical Michaelis-Menten kinetics [25, 24, 18]

$$S_{ex}(C_{ex}) = S_{ex}^{max}\frac{C_{ex}}{C_{ex}+C_{1/2}}, \tag{25}$$

where S_{ex}^{max} and $C_{1/2}$ are two parameters for the maximum consumption rate and concentration at half-max consumption. Detailed models will be given below for in-domain and inter-domain fluxes J_j^r and $S_{i,j}$, as well as the boundary conditions.

2.2.1. In-domain oxygen flux

The in-domain oxygen fluxes in the four domains Ω_j $(j = ai, ao, v, ex)$ consist of convective and diffusive terms

$$\begin{aligned} J_k^r &= \bar{C}_k u_k^r - D_k\tau_k\frac{\partial C_k}{\partial r}, \quad k = ai, ao, v, \\ J_{ex}^r &= C_{ex}u_{ex}^r - D_{ex}\tau_{ex}\frac{\partial C_{ex}}{\partial r}, \end{aligned} \tag{26}$$

where D_j, τ_j, u_j^r $(j = ai, ao, v, ex)$ are the diffusion constant of oxygen, the tortuosity, and the blood/water velocity defined in (2,4).

2.2.2. Oxygen exchange through blood vessel wall

The oxygen exchange rate per unit volume from Ω_j to Ω_{ex} follows

$$S_{j,ex} = M_{j,ex}J_{j,ex}, \quad j = ai, ao, v, ci, co, \tag{27}$$

where $M_{j,ex}$ is defined in (6). The oxygen flux $J_{j,ex}$ per unit area is modeled by

$$J_{j,ex} = l_{j,ex}(C_j - C_{ex}) + U_{j,ex}C_{j,ex}^{upwind}, \quad j = ai, ao, v, ci, co, \tag{28}$$

where $U_{j,ex}$ is defined in (7), $l_{j,ex}$ is the oxygen permeability through the blood vessel wall [25, 20], and $C_{j,ex}^{upwind}$ is the upwind or upstream concentration determined by the sign of $U_{j,ex}$. Combining (27,28) with the use of (5), we obtain

$$S_{j,ex} = M_{j,ex}l_{j,ex}(C_j - C_{ex}) + Q_{j,ex}C_{j,ex}^{upwind}, \quad j = ai, ao, v, ci, co, \tag{29}$$

and $C_{j,ex}^{upwind}$ is given by

$$C_{j,ex}^{upwind} = \begin{cases} C_j & \text{if } Q_{j,ex} \geq 0, \\ C_{ex} & \text{if } Q_{j,ex} < 0. \end{cases} \tag{30}$$

2.2.3. Oxygen exchange between vascular domains

The oxygen exchange rates between capillaries and other vascular domains are

$$\begin{aligned} S_{ai,ci} &= Q_{ai,ci}\bar{C}_{ai} + D_{ai,ci}(C_{ai} - C_{ci}), \quad S_{ao,co} = Q_{ao,co}\bar{C}_{ao} + D_{ao,co}(C_{ao} - C_{co}), \\ S_{v,ci} &= Q_{v,ci}\bar{C}^{upwind}_{ci,v} + D_{v,ci}(C_v - C_{ci}), \quad S_{v,co} = Q_{v,co}\bar{C}^{upwind}_{co,v} + D_{v,co}(C_v - C_{co}), \end{aligned} \tag{31}$$

where $D_{i,j}$ are effective diffusion constants between domains (estimated in Appendix A.2), the $Q_{i,j}$ terms are defined in (8), and $\bar{C}^{upwind}_{k,v}$ $(k = ci, co)$ is the total oxygen concentration before entering to Ω_v. We take $\bar{C}^{upwind}_{ci,v}$ for example. One simple option is $\bar{C}^{upwind}_{ci,v} = \bar{C}_{ci}$, but this does not consider the possible gradient inside the capillary network point. If there is more than sufficient oxygen supply for exchange to the extravascular domain, we assume a linear decreasing profile for dissolved oxygen concentration C_{ci} within a point (network) in the capillary domain, which implies

$$C^{upwind}_{ci,v} = 2C_{ci} - C_{ai}, \quad \text{if} \quad C^{upwind}_{ci,v} > C_{ex}. \tag{32}$$

When the above $C^{upwind}_{ci,v} \le C_{ex}$, the capillary domain cannot supply oxygen through the permeability term in (28) so the concentration will not decrease further. In summary, we adopt the model

$$C^{upwind}_{ci,v} = \max\{2C_{ci} - C_{ai}, C_{ex}\}, \tag{33}$$

and define

$$\bar{C}^{upwind}_{ci,v} = \bar{C}(C^{upwind}_{ci,v}, H_{ci}), \tag{34}$$

by using the function in (22). Similarly, $\bar{C}^{upwind}_{co,v}$ can be defined by replacing subscripts ci, ai by co, ao.

2.2.4. Boundary conditions

Now we propose boundary conditions for both H_k $(k = ai, ao, v)$ and C_j $(j = ai, ao, v, ex)$ at $r = R_0, R_1$. For the H_k, we have

$$\begin{aligned} &H_{ai}(R_0, t) = H_0, \quad \frac{\partial H_{ai}}{\partial r}(R_1, t) = 0, \\ &\frac{\partial H_{ao}}{\partial r}(R_0, t) = 0, \quad H_{ao}(R_1, t) = H_0, \\ &\frac{\partial H_v}{\partial r}(R_0, t) = 0, \quad \frac{\partial H_v}{\partial r}(R_1, t) = 0, \end{aligned} \tag{35}$$

where H_0 is the averaged oxygen-binding capacity of blood under normal conditions (see Table A.9), and all the Neumann conditions imply that hemoglobins (or RBC) can not flow out these boundaries consistent with flow boundary conditions (12,14,16). For the concentrations, we have

$$\begin{aligned} &C_{ai}(R_0,t) = C_{ai,0}, \quad \frac{\partial C_{ai}}{\partial r}(R_1,t) = 0, \\ &\frac{\partial C_{ao}}{\partial r}(R_0,t) = 0, \quad C_{ao}(R_1,t) = C_{ao,1}, \\ &\frac{\partial C_v}{\partial r}(R_0,t) = 0, \quad \frac{\partial C_v}{\partial r}(R_1,t) = 0, \\ &\frac{\partial C_{ex}}{\partial r}(R_0,t) = 0, \quad \frac{\partial C_{ex}}{\partial r}(R_1,t) = 0, \end{aligned} \tag{36}$$

where $C_{ai,0}$ and $C_{ao,1}$ are given dissolved oxygen concentrations at arteries CRA and PCA. Neumann conditions are adopted for other conditions, which will not have much effect on numerical results, since the in-domain diffusive terms are very small compared with the convective terms by fluid flow.

2.3. Nondimensionalization

2.3.1. The water/blood circulation

We adopt the scalings

$$\begin{aligned} &\tilde{t} = \frac{t}{t_0}, \quad \tilde{r} = \frac{r}{R_1}, \quad \tilde{p}_k = \frac{p_k}{P_{v,0}}, \quad \tilde{\pi}_k = \frac{\pi_k}{P_{v,0}}, \\ &\tilde{P}_k^{re} = \frac{P_k^{re}}{P_{v,0}}, \quad \tilde{Q}_{j,k} = Q_{j,k} t_0, \quad \tilde{\lambda}_j = \frac{\lambda_j}{P_{v,0}}. \end{aligned} \tag{37}$$

The time scale t_0 is chosen to be

$$t_0 = 1\,\text{mm}/(10\,\text{mm/s}) = 0.1\text{s}, \tag{38}$$

where typical length scale 1mm is chosen based on the scale of maximum radius $R_1 = 0.79\,$mm for the domain, and the typical velocity scale $10\,$mm/s is chosen based on some typical blood flow velocity in [16]. The above choice will also give $O(1)$ dimensionless velocity for the in-domain blood flows. Substituting the above scalings in the system in Section 2.1 and after removing the tilde for the unknown variables $\tilde{p}_k, \tilde{Q}_{j,k}$ and independent variables $\tilde{r}, \tilde{t}$ for

mathematical simplicity, we have the dimensionless system

$$\begin{aligned}
&\frac{\partial \eta_{ai}}{\partial t} - \frac{1}{r}\frac{\partial}{\partial r}\left(\bar{\kappa}_{ai} r \frac{\partial p_{ai}}{\partial r}\right) + Q_{ai,ex} + Q_{ai,ci} = 0,\\
&\frac{\partial \eta_{ao}}{\partial t} - \frac{1}{r}\frac{\partial}{\partial r}\left(\bar{\kappa}_{ao} r \frac{\partial p_{ao}}{\partial r}\right) + Q_{ao,ex} + Q_{ao,co} = 0,\\
&\frac{\partial \eta_{v}}{\partial t} - \frac{1}{r}\frac{\partial}{\partial r}\left(\bar{\kappa}_{v} r \frac{\partial p_{v}}{\partial r}\right) + Q_{v,ex} + Q_{v,ci} + Q_{v,co} = 0,\\
&\frac{\partial \eta_{ci}}{\partial t} + Q_{ci,ex} - Q_{ai,ci} - Q_{v,ci} = 0,\\
&\frac{\partial \eta_{co}}{\partial t} + Q_{co,ex} - Q_{ao,co} - Q_{v,co} = 0,\\
&\frac{\partial}{\partial r}\left(\sum_{k=v,ai,ao,ex} \bar{\kappa}_k r \frac{\partial p_k}{\partial r}\right) = 0,
\end{aligned} \tag{39}$$

where the water/blood flow rates are

$$\begin{aligned}
&Q_{j,ex} = \bar{L}_{j,ex}\left[p_j - p_{ex} - (\tilde{\pi}_j - \tilde{\pi}_{ex})\right], \quad j = ai, ao, v, ci, co\\
&Q_{k,ci} = \bar{K}_{k,ci}(p_k - p_{ci}), \quad k = ai, v,\\
&Q_{k,co} = \bar{K}_{k,co}(p_k - p_{co}), \quad k = ao, v,
\end{aligned} \tag{40}$$

and the parameters are

$$\begin{aligned}
&\bar{L}_{j,ex} = \tilde{L}_{j,ex}\sqrt{\eta_j}, \quad \tilde{L}_{j,ex} = M^0_{j,ex} L_{j,ex} P_{v,0} t_0, \quad j = ai, ao, v, ci, co,\\
&\bar{\kappa}_j = \tilde{\beta}_j \eta_j^2, \quad \tilde{\beta}_j = \frac{\beta_j \tau_j P_{v,0} t_0}{8 R_1^2 \mu_b}, \quad j = ai, ao, v,\\
&\bar{\kappa}_{ex} = \tilde{\kappa}_{ex}\eta_{ex}, \quad \tilde{\kappa}_{ex} = \frac{P_{v,0}\kappa_{ex}\tau_{ex} t_0}{R_1^2 \mu_{ex}},\\
&\bar{K}_{j,ci} = \frac{\bar{K}_j \bar{K}_{ci}}{\bar{K}_j + \bar{K}_{ci}}, \quad j = ai, v, \quad \bar{K}_{j,co} = \frac{\bar{K}_j \bar{K}_{co}}{\bar{K}_j + \bar{K}_{co}}, \quad j = ao, v\\
&\bar{K}_j = \tilde{\delta}_j \eta_j^2 \frac{\bar{\epsilon}_j}{\tanh(\bar{\epsilon}_j)}, \quad \bar{\epsilon}_j = \frac{1}{2}\eta_j^{-3/4}\sqrt{\tilde{L}_{j,ex}/\tilde{\delta}_j}, \quad j = ai, ao, v, ci, co.\\
&\tilde{\delta}_j = \delta_j P_{v,0} t_0, \quad j = ai, ao, v, ci, co.
\end{aligned} \tag{41}$$

In the above notations (and in the next subsection), the quantities with a bar (e.g. $\bar{\kappa}_j$) are effective coefficients and depend on the unknown variables (e.g.,

η_j), whereas quantities with a tilde (e.g., $\tilde{\beta}_j$) are dimensionless parameters that do not depend the unknowns. The algebraic constraint for volume fractions is

$$\eta_{ai} + \eta_{ao} + \eta_v + \eta_{ex} + \eta_{ci} + \eta_{co} = 1, \tag{42}$$

and the force balance constraint is given by

$$\tilde{\lambda}_j(\eta_j - \eta_j^{re}) = p_j - p_{ex} - (\tilde{P}_j^{re} - \tilde{P}_{ex}^{re}), \quad j = ai, ao, v, ci, co. \tag{43}$$

The dimensionless form for the boundary conditions in Section 2.1.5 will have the same form except that the given pressures are nondimentionalized and the dimensionless domain is $r \in [\tilde{R}_0, \tilde{R}_1]$ with $\tilde{R}_1 = 1$. The dimensionless flow rates conditions in (13,15) have the form

$$-\bar{\kappa}_{ao} r \frac{\partial p_{ao}}{\partial r}\bigg|_{r=\tilde{R}_1=1} = -Q_{ao}^*, \quad -\bar{\kappa}_{ai} r \frac{\partial p_{ai}}{\partial r}\bigg|_{r=\tilde{R}_0} = Q_{ai}^*. \tag{44}$$

2.3.2. The oxygen transport

We adopt the scalings

$$\begin{aligned} &\tilde{t} = \frac{t}{t_0}, \quad \tilde{r} = \frac{r}{R_1}, \quad \tilde{C}_k = \frac{C_k}{C_{ai,0}}, \quad \tilde{\bar{C}}_k = \frac{\bar{C}_k}{C_{ai,0}}, \quad \tilde{H}_k = \frac{H_k}{C_{ai,0}}, \\ &\tilde{S}_{ex}^{max} = \frac{S_{ex}^{max} t_0}{C_{ai,0}}, \quad \tilde{C}_{50} = \frac{C_{50}}{C_{ai,0}}, \quad \tilde{C}_{1/2} = \frac{C_{1/2}}{C_{ai,0}}, \end{aligned} \tag{45}$$

The timescale t_0 is the same as in (38), since the in-domain diffusion timescale $R_1^2/D_k \sim 10^3$s is much larger. Substituting the scalings and after removing the tilde for the unknowns $\tilde{H}_k, \tilde{C}_k, \tilde{\bar{C}}_k$ and independent variables $\tilde{t}, \tilde{r}$, we have the equations for H_k

$$\begin{aligned} &\frac{\partial(\eta_{ai} H_{ai})}{\partial t} - \frac{1}{r}\frac{\partial}{\partial r}\left(\bar{\kappa}_{ai} r \frac{\partial p_{ai}}{\partial r} H_{ai}\right) + Q_{ai,ci} H_{ai} = 0, \\ &\frac{\partial(\eta_{ao} H_{ao})}{\partial t} - \frac{1}{r}\frac{\partial}{\partial r}\left(\bar{\kappa}_{ao} r \frac{\partial p_{ao}}{\partial r} H_{ao}\right) + Q_{ao,co} H_{ao} = 0, \\ &\frac{\partial(\eta_v H_v)}{\partial t} - \frac{1}{r}\frac{\partial}{\partial r}\left(\bar{\kappa}_v r \frac{\partial p_v}{\partial r} H_v\right) + Q_{v,ci} H_{ci} + Q_{v,co} H_{co} = 0, \\ &\frac{\partial(\eta_{ci} H_{ci})}{\partial t} - Q_{ai,ci} H_{ai} - Q_{v,ci} H_{ci} = 0, \\ &\frac{\partial(\eta_{co} H_{co})}{\partial t} - Q_{ao,co} H_{ao} - Q_{v,co} H_{co} = 0, \end{aligned} \tag{46}$$

and the equations for $\bar{C}_k$ and C_{ex}

$$\begin{aligned}
&\frac{\partial}{\partial t}(\eta_{ai}\bar{C}_{ai}) - \frac{1}{r}\frac{\partial}{\partial r}\left(\bar{\kappa}_{ai}\bar{C}_{ai}r\frac{\partial p_{ai}}{\partial r} + \bar{D}_{ai}r\frac{\partial C_{ai}}{\partial r}\right) + S_{ai,ex} + S_{ai,ci} = 0,\\
&\frac{\partial}{\partial t}(\eta_{ao}\bar{C}_{ao}) - \frac{1}{r}\frac{\partial}{\partial r}\left(\bar{\kappa}_{ao}\bar{C}_{ao}r\frac{\partial p_{ao}}{\partial r} + \bar{D}_{ao}r\frac{\partial C_{ao}}{\partial r}\right) + S_{ao,ex} + S_{ao,co} = 0,\\
&\frac{\partial}{\partial t}(\eta_{v}\bar{C}_{v}) - \frac{1}{r}\frac{\partial}{\partial r}\left(\bar{\kappa}_{v}\bar{C}_{v}r\frac{\partial p_{v}}{\partial r} + \bar{D}_{v}r\frac{\partial C_{v}}{\partial r}\right) + S_{v,ex} + S_{v,ci} + S_{v,co} = 0,\\
&\frac{\partial}{\partial t}(\eta_{ci}\bar{C}_{ci}) + S_{ci,ex} - S_{ai,ci} - S_{v,ci} = 0,\\
&\frac{\partial}{\partial t}(\eta_{co}\bar{C}_{co}) + S_{co,ex} - S_{ao,co} - S_{v,co} = 0,\\
&\frac{\partial}{\partial t}(\eta_{ex}C_{ex}) - \frac{1}{r}\frac{\partial}{\partial r}\left(\bar{\kappa}_{ex}C_{ex}r\frac{\partial p_{ex}}{\partial r} + \bar{D}_{ex}r\frac{\partial C_{ex}}{\partial r}\right) + S_{ex} - \sum_{j=ai,ao,v,ci,co} S_{j,ex} = 0,
\end{aligned} \tag{47}$$

where total oxygen concentration $\bar{C}_k$ is

$$\bar{C}_k(C_k, H_k) = C_k + H_k\frac{C_k^n}{C_k^n + \tilde{C}_{50}^n}, \quad k = ai, ao, v, ci, co, \tag{48}$$

the oxygen exchange and consumption rates are given by

$$\begin{aligned}
&S_{j,ex} = Q_{j,ex}C_{j,ex}^{upwind} + \bar{l}_{j,ex}(C_j - C_{ex}), \quad j = ai, ao, v, ci, co,\\
&S_{ai,ci} = Q_{ai,ci}\bar{C}_{ai} + \tilde{D}_{ai,ci}(C_{ai} - C_{ci}),\\
&S_{ao,co} = Q_{ao,co}\bar{C}_{ao} + \tilde{D}_{ao,co}(C_{ao} - C_{co}),\\
&S_{v,k} = Q_{v,k}\bar{C}_{k,v}^{upwind} + \tilde{D}_{v,k}(C_v - C_k), \quad k = ci, co,\\
&S_{ex} = \tilde{S}_{ex}^{max}\frac{C_{ex}}{C_{ex} + \tilde{C}_{1/2}},
\end{aligned} \tag{49}$$

and the coefficients are defined by

$$\begin{aligned}
&\bar{D}_j = \tilde{D}_j\eta_j, \quad \tilde{D}_j = \frac{D_j\tau_j t_0}{R_1^2}, \quad j = ai, ao, v, ex,\\
&\bar{l}_{j,ex} = \tilde{l}_{j,ex}\sqrt{\eta_j}, \quad \tilde{l}_{j,ex} = M_{j,ex}^0 l_{j,ex}t_0, \quad j = ai, ao, v, ci, co,\\
&\tilde{D}_{j,ci} = D_{j,ci}t_0, \quad j = ai, v, \quad \tilde{D}_{j,co} = D_{j,co}t_0, \quad j = ao, v.
\end{aligned} \tag{50}$$

The boundary conditions in (35,36) will take the same form except that $C_{ai,0}, C_{ao,1}, H_0$ are nondimensionalized by $C_{ai,0}$.

3. Numerical Results

In our implementation, the partial differential equations in (39), (46),(47) with boundary conditions are converted to dynamic systems by using the finite-difference method for the spatial variable r. In the finite-difference scheme, the upwind scheme is used for the convective terms in (46) and (47) (otherwise it is unstable) and central discretization is adopted for other terms. Then, they are solved as a whole system of differential-algebraic equations (DAE) by combining with the algebraic constraints (42),(43),(48). The DAE system is solved in Matlab using the built-in solver ode15s. All the 28 unknowns p_k, η_k, C_k $(k = ai, ao, v, ci, co, ex)$ and $\bar{C}_j, H_j$ $(j = ai, ao, v, ci, co)$ at all discrete spatial points are solved simultaneously. In this section, we consider a uniform case that resting volume fractions $\eta_j^{re}(r)$ $(j = ai, ao, v, ci, co, ex)$ follow uniform distribution, i.e., they are assumed to be constants. All the chosen parameters are given/estimated in Appendix A. This case will serve as a reference case for the study of the effects of resting volume fractions and other parameters in the next section.

3.1. Water/blood circulation

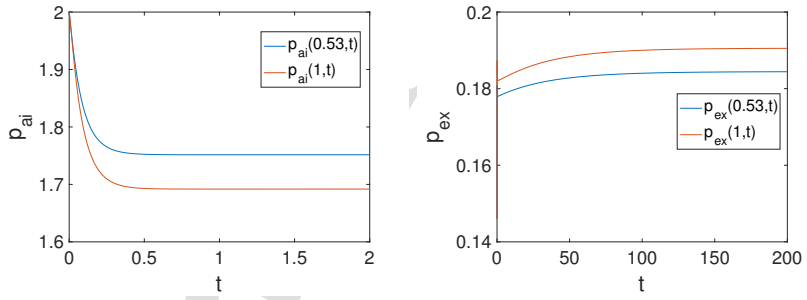

(a) (b)

Figure 2: The dynamics of p_{ai} and p_{ex} at two points $r = 0.53, 1$.

The values used in the initial conditions at $t = 0$ are set to be consistent with the algebraic constraints and the boundary conditions for pressures. At $t = 2$, most of the unknowns have reached the steady state. Figure 2(a) shows the dynamics of artery pressure p_{ai} at two locations $r = 0.53, 1$. The pressure

p_{ex} in Figure 2(b) reaches the steady state slower (at about $t = 200$), because it is more sensitive to the small variations of volume fractions η_k during the dynamics via the effective permeability $\bar{\kappa}_k$ in $(39)_6$.

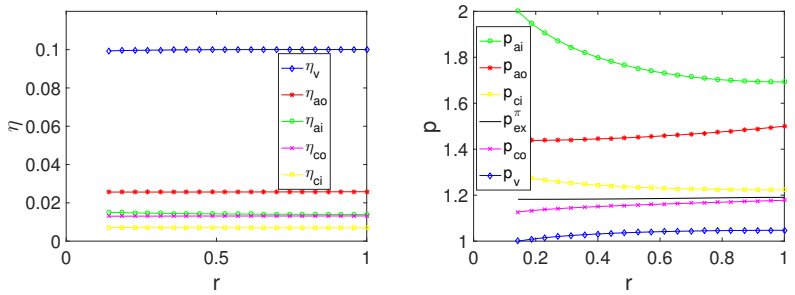

(a) (b)

Figure 3: The spatial profiles of (a) volume fractions η_j and (b) pressures p_j in domain Ω_j at steady state.

Next, we illustrate the steady-state profiles with $t = 200$ in the dimensionless geometric region $0.14 < r < 1$. Figure 3(a) shows profiles of volume fractions in the five vascular domains, which are almost uniform since the difference $\eta_k - \eta_k^{re}$ is quite small (with max around 2.5×10^{-3}) due to the large moduli $\tilde{\lambda}_k$. The remaining percentage of about 85% is for η_{ex} (not shown in the figure). Figure 3(b) shows the pressures in the six domains, where for convenience of comparison we have defined

$$p_{ex}^{\pi} = p_{ex} + \Delta\tilde{\pi} = p_{ex} + \tilde{\pi}_v - \tilde{\pi}_{ex}. \tag{51}$$

It shows that the pressures in the two artery domains drop along the direction of blood flow, and the pressure in capillary domain lies between the connected artery and vein domains. The modified extravascular pressure p_{ex}^{π} lies between the artery and vein pressures, and the sign of the difference between p_{ex}^{π} and vascular pressures will determine the direction of water leak through blood vessel wall.

Figure 4(a) shows the blood flow rates going through capillaries between the vascular domains. These are the dominant terms in the governing equations in (39) and are to be balanced with the in-domain flows through arteries and veins. The signs of $Q_{i,j}$ in Figure 4(a) indicate that blood flows from

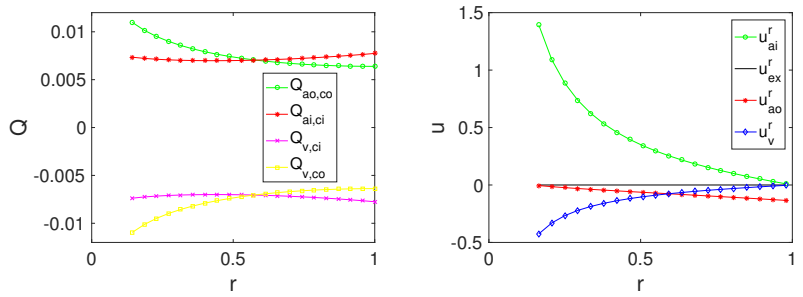

(a) (b)

Figure 4: (a) Blood flow rates between vascular domains; (b) In-domain velocities.

artery to capillary and then from capillary to vein. Figure 4(b) shows the dimensionless in-domain blood/water velocities, which are defined as

$$u_j^r = -\tilde{\beta}_j \eta_j \frac{\partial p_j}{\partial r}, \quad j = ai, ao, v, \quad u_{ex}^r = -\tilde{\kappa}_{ex} \frac{\partial p_{ex}}{\partial r}. \tag{52}$$

The sign of velocity in Figure 4(b) is consistent with the pressure drops in Figure 3(b) and we have the following expected observations

- for Ω_{ai}, blood flows from inner boundary $r = R_0$ (i.e., the CRA) to outer boundary $r = R_1$ with decreasing velocity;
- for Ω_{ao}, blood flows from outer boundary (i.e., the PCA) to the inner boundary with decreasing velocity;
- for Ω_v, blood flows from the outer boundary to the inner boundary (i.e., the CRV) with increasing velocity;
- the water flow in Ω_{ex} is negligibly small compared with scale of blood flow.

The maximum velocity occurs at the start of artery (CRA) in Ω_{ai}, where the pressure drop is most significant. The velocity at inner boundary in Ω_v is also relatively large, since the blood will eventually merge and drain from the system through the CRV. The scaling factor for the velocity is

$$\frac{R_1}{t_0} = 0.79\,\text{cm/s}, \tag{53}$$

and the maximum velocity with units in this case is 1.1 cm/s, consistent with the scales in [14, 26, 25, 43]. Figure 5 shows the water flow rates across the blood vessel wall, which are much smaller than the blood flow rates in Figure 4(a). This is expected with the chosen parameters under normal physiological conditions, but the water flow rates could change significantly under pathological conditions.

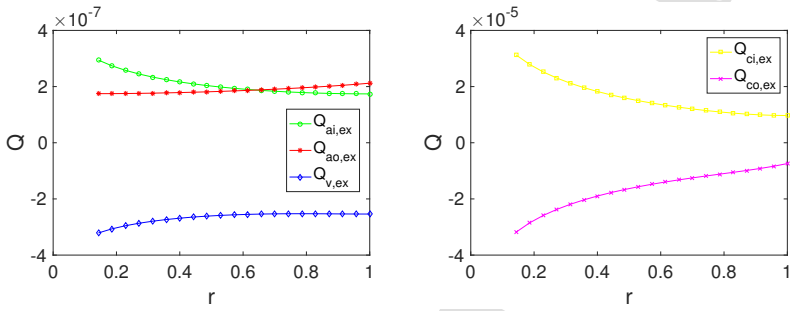

(a) (b)

Figure 5: The water flow rates across the blood vessel wall between (a) the vascular domains and (b) the extravascular domain.

3.2. Oxygen transport

To better understand the numerical results, we first show the quantities $\bar{C}_k$ in (48) for the vascular domains and S_{ex} in $(49)_5$ (or equation (25) in dimensional form) for the extravascular domain. Figure 6(a) shows relation between the total concentration $\bar{C}_k$ and dissolved concentration C_k with $H_k = H_0 = 66.7$ in vascular domains, which implies that the majority of the oxygen is stored in the RBCs. With $C_k = 1$, we have $\bar{C} \approx 66$, so the dissolved oxygen is only about 1.5% of the total oxygen while the oxygen stored in RBC is about 98.5% as expected [7]. Figure 6(b) shows the relation between the normalized oxygen consumption rate $S_{ex}/\tilde{S}_{ex}^{max}$ and the oxygen concentration C_{ex} with $\tilde{C}_{1/2} = 0.016$, showing that the consumption rate is maintained at relatively high level (e.g., above 95% of maximum) if C_{ex} is maintained at reasonable values (e.g., $C_{ex} > 0.3$). The parameter $\tilde{S}_{ex}^{max}$ in the formula $(49)_5$ or the dimensional parameter S_{ex}^{max} in (25) is estimated in Appendix A.2.

Figure 7(a) shows the dynamics of concentrations at a middle point $r = 0.53$, which implies that they already reach the steady state at $t = 200$.

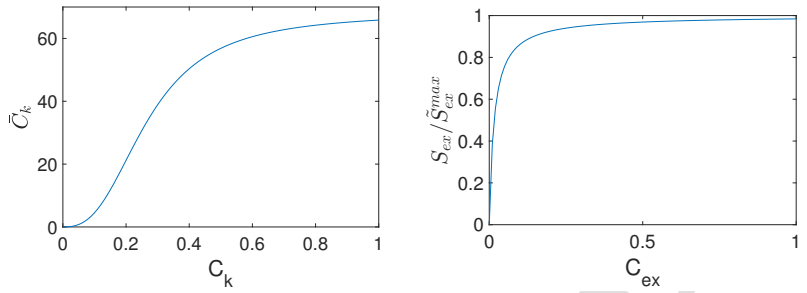

(a) (b)

Figure 6: (a) Relation between total concentration $\bar{C}_k$ and dissolved concentration C_k by (48); (b) Relation between consumption rate $S_{ex}/\tilde{S}_{ex}^{max}$ and dissolved concentration C_{ex} in tissue by $(49)_5$.

Figure 7(b) shows the profiles of dissolved concentrations C_k in six domains at steady state (at $t = 200$). The highest two curves are for the two artery domains, and the concentrations decrease along the direction of blood flow. The middle two curves for the capillary domains lie between those for the artery and vein domains. This is expected since the major exchange and supply of oxygen occur via the capillary domains. The oxygen concentrations in the vein and extravascular domains have similar values and are the lowest among the domains. Figure 7(c) shows the upwind concentrations $C_{co,v}^{upwind}, C_{ci,v}^{upwind}$ before entering into the vein domain (see (33)), and in this reference case they are equal to C_{ex}. The total oxygen concentrations in Figure 7(d) follow similar shape as in Figure 7(b), but at a much larger order of magnitude.

Figure 8 shows the oxygen exchange rates between different domains, including the diffusion mechanisms (related to $\tilde{D}_{i,j}$ and $\bar{l}_{i,j}$) and the convection mechanisms (related to blood/water flows $Q_{i,j}$). In the vascular domains, the oxygen exchange follows the direction of blood flow from artery to capillary and then to vein since $S_{ai,ci}, S_{ao,co}$ are positive and $S_{v,ci}, S_{v,co}$ are negative in Figure 8(a,b). In addition, the convection dominates the exchange process in vasculature since the order of magnitude in Figure 8(a) due to diffusion is negligibly small compared with that in Figure 8(b) due to convection.

The supply of oxygen to the extravascular domain is mainly through

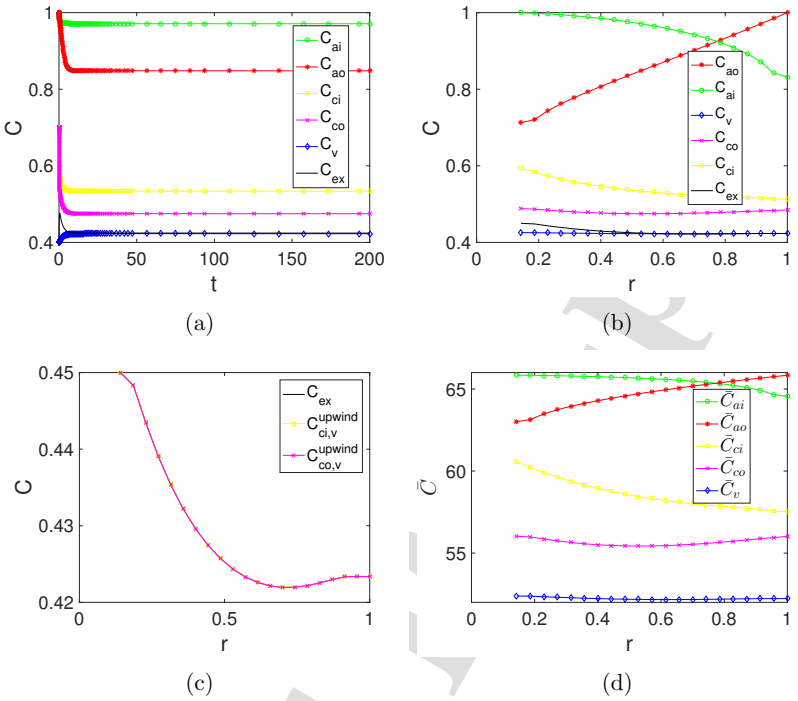

Figure 7: Dynamics of concentrations at $r = 0.53$ and the steady-state profiles of concentrations.

diffusion across the blood vessel wall compared with convection, shown in Figure 8(c,d). Figure 8(c) also shows that the two capillary domains provide the major supply of oxygen to the extravascular domain, and the total consumption rate S_{ex} per unit volume is relatively stable. The drop for C_k ($k = ai, ao$) in artery domains in Figure 7(b) is also due to the diffusion of oxygen through blood vessel wall.

In summary, in the present model, the pathway of supply of oxygen is mainly by convection, from artery to the capillary, and by diffusion, to the extravascular domain (tissue) consistent with common sense.

Figure 9(a) shows the profiles of oxygen binding capacity H_k in vascular domains, indicating that they are almost a constant (i.e., H_0) for all five vascular domains, which verifies the argument that they can be assumed as

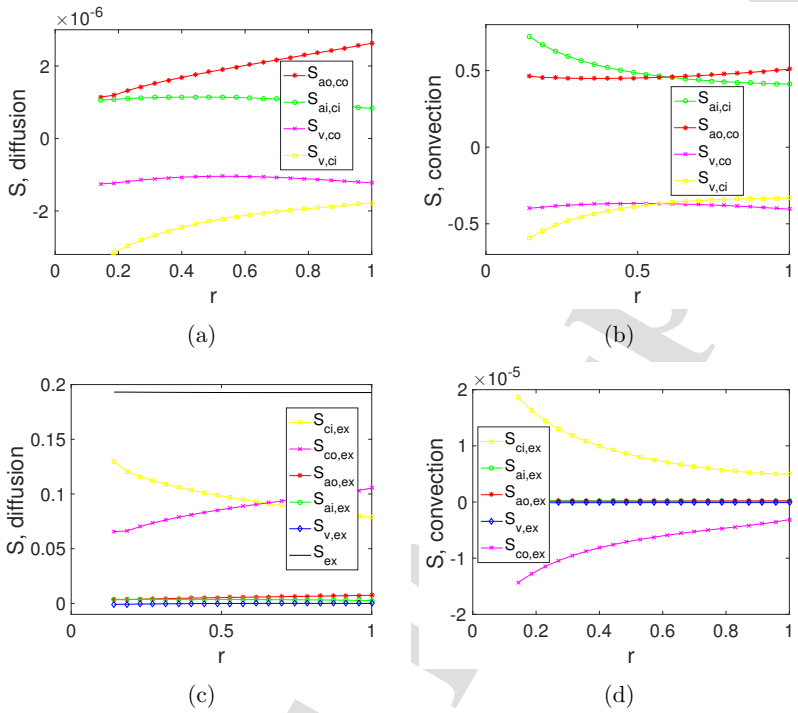

Figure 8: Oxygen exchange rates between different domains due to diffusion and convection mechanisms.

a constant under the normal physiological conditions when water leak across blood vessel wall is small. Figure 9(b) shows the profiles of oxygen saturation S_{O_2} in the five vascular domains, which are quite similar in shapes to those in Figure 7(d) since they almost differ by a scaling factor H_0. At a fixed location, there is oxygen saturation drop (about 20 %) from artery to vein through the capillary, due to capillary oxygen exchanges by diffusion (see Figure 8(c)). For example, at $r = 0.53$, the oxygen saturation drops by 19% (from 97% to 78%) from artery Ω_{ai} to vein Ω_v through capillary Ω_{ci}. When it is multiplied by H_{ci}, the bound-oxygen drops by 12.8, more than 20 times the drop of the dissolved oxygen 0.55 (from 0.97 to 0.42). The oxygen supply is mainly released from the bound oxygen stored in the hemoglobin in RBCs.

In summary, for the reference case with uniform distribution of resting

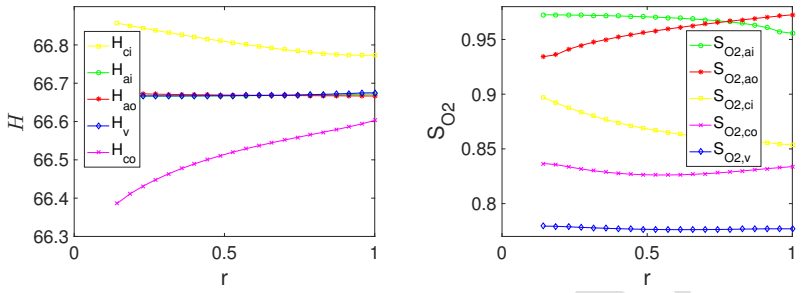

(a) (b)

Figure 9: The steady-state profiles of (a) oxygen binding capacity H_k and (b) oxygen saturation $S_{O2,k} = C_k^n/(C_k^n + \tilde{C}_{50}^n)$ in (48) in the five vascular domains

volume fractions, the blood supply and oxygen delivery is sufficient and stable from the two sets of vasculature networks, and the pathways are as expected.

4. Effects and sensitivity of parameters

4.1. Effects of resting volume fractions

The resting volume fractions $\eta_j^{re}(r)$ in (43) depend on the structural information of blood vessels. Without detailed information, we assumed uniform (constant) profile for $\eta_j^{re}(r)$ in the previous section. We now consider two cases with different volume fraction profiles.

In the first case, we assume a Gaussian profile for $\eta_j^{re}(r)$, called Gaussian case 1 later. On the one hand, when the main branch of blood vessel divides into two sub-branches, the total cross sectional area of blood vessel will increase (e.g., 1.2 fold), so the volume fractions will increase according to the level of branches; on the other hand, some branches will terminate at a certain length, so the volume fractions will decrease after a certain branching level. We assume that the two artery resting volume fractions follow a Gaussian profile with different means and standard deviations.

$$\eta_{ai}^{re}(r) \sim \mathcal{N}(0.4, 0.2), \quad \eta_{ao}^{re}(r) \sim \mathcal{N}(0.7, 0.2). \tag{54}$$

Roughly speaking, the maximum is located at about 1/3 of the domain from the start of artery. Suppose the capillaries and the vein at resting state are

responding to the profiles of the two sets of arteries

$$\eta_{ci}^{re} \sim \mathcal{N}(0.4, 0.2), \quad \eta_{co}^{re} \sim \mathcal{N}(0.7, 0.2), \quad \eta_{v}^{re} \sim \eta_{ci}^{re} + \eta_{co}^{re}. \tag{55}$$

A scaling constant will be multiplied on the profiles of each volume fraction η_j $(j = ai, ao, ci, co, v)$ to ensure the weighted average value over the whole domain is the same as those in the uniform case.

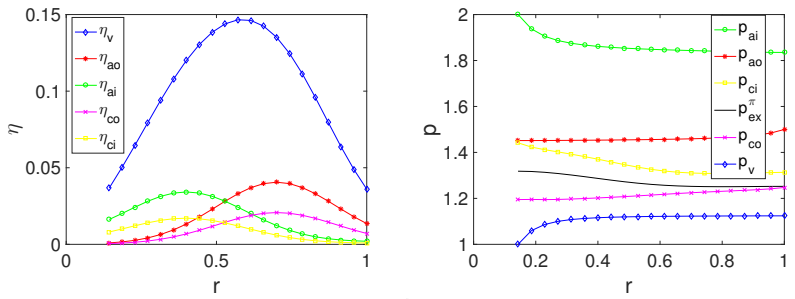

(a) (b)

Figure 10: Profiles of volume fractions and pressures at steady state in Gaussian case 1.

The volume fractions η_j at steady state (at $t = 200$) are shown in Figure 10(a), which follow similar resting Gaussian profiles for η_j^{re}, since the difference $\eta_j - \eta_j^{re}$ is quite small (with max around 3×10^{-3}) due to the large moduli $\tilde{\lambda}_j$.

Figure 10(b) shows the pressure profiles, where one major difference from the uniform case is that the total pressure drop in the artery domain Ω_{ai} is smaller but that in vein domain Ω_v is larger.

Figure 11(a) shows the flow rates between capillary domains and other vascular domains, which follow similar Gaussian profiles as the volume fractions in each capillary domain, e.g., the maximum values are also aligned at similar spatial locations $r = 0.4, 0.7$. The in-domain velocities in Figure 11(b) follow a trend similar to the uniform case, but the velocity in vein Ω_v is larger at $r = R_0$ since the volume fraction (equivalently total cross-sectional area) η_v is much smaller at $r = R_0$ than that in the uniform case. Table 2 shows the average values of these flows rates in Figure 11(a) and the two artery boundary flow rates defined in (44), for this Gaussian case 1 in comparision with uniform case. The change in average values is partly due to

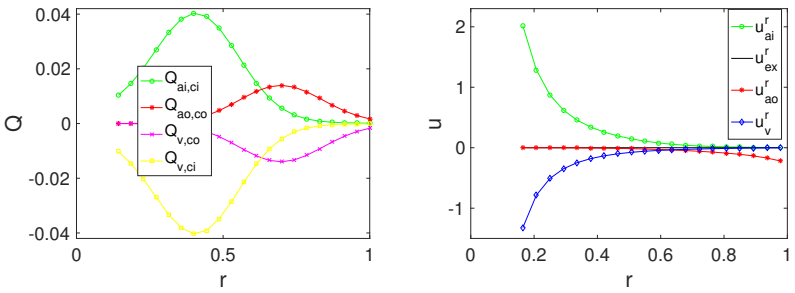

(a) (b)

Figure 11: The flow rates and velocities in the Gaussian case 1

the fact that Ω_{ao} contributes more to inner region (small r) while Ω_{ai} contributes more to outer region. The blood supply from the Ω_{ai} boundary (i.e., the CRA) is significantly increased, while that from the Ω_{ao} boundary (i.e., the PCA) stays almost the same. Therefore, the resting volume fractions strongly affects the blood supply and exchanges in the vasculature.

	$Q_{ai,ci}, \lvert Q_{v,ci}\rvert$	$Q_{ao,co}, \lvert Q_{v,co}\rvert$	Q^*_{ai}	Q^*_{ao}
Uniform Case	0.0076	0.0072	0.0034	0.0034
Gaussian case 1	0.0164	0.0055	0.0060	0.0034
Gaussian case 2	0.0332	0.0068	0.0090	0.0038

Table 2: Average values of capillary flow rates over the whole region and the two artery boundary flow rates in three cases.

For the oxygen transport part, Figure 12 shows the profiles of C_k and H_k at steady state ($t = 200$). Figure 12(a) shows larger variations for the concentrations compared with the uniform case, where the low concentration of C_{ex} near $r = 1$ indicates an insufficient supply of oxygen there. Figure 12(b) shows that H_k in arteries and veins are almost the normal constant H_0, but the H_{ci}, H_{co} in capillary domains near the boundary has significant variations since the water leak is comparable with the small blood exchanges there.

The pathways of oxygen supply to the extravascular domain are similar to the previous uniform case, but Figure 13 shows larger spatial variations

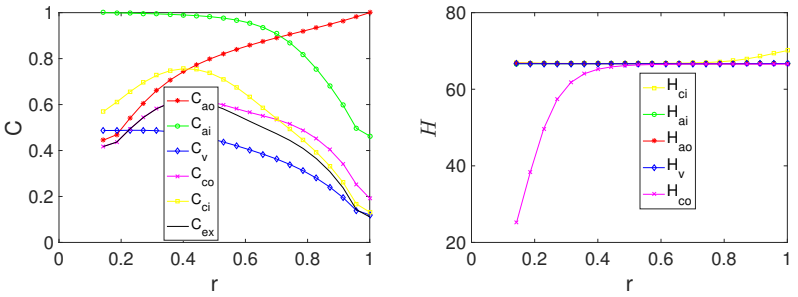

(a) (b)

Figure 12: The profiles of C_k, H_k at steady state $t = 200$, with Gaussian case 1.

for oxygen exchange rates in different domains. The oxygen exchange in Figure 13(a) between capillary and other vascular domains follows Gaussian-like profiles since it is convection dominant (see Figure 11(a)). Figure 13(b) shows that the terms $S_{ci,ex}, S_{co,ex}$ in two capillary sets serve different regions, one for the inner and the other for the outer region, and their sum is almost the total oxygen consumption S_{ex}. The total oxygen consumption S_{ex} has a dip of about 10% near $r = 1$, which means the insufficient supply of oxygen in that region, consistent with small C_{ex} in Figure 12(a).

In the second case, called Gaussian case 2, we consider

$$\begin{aligned} &r\eta_{ai}^{re}(r) \sim \mathcal{N}(0.4, 0.2), \quad r\eta_{ao}^{re}(r) \sim \mathcal{N}(0.7, 0.2), \\ &r\eta_{ci}^{re} \sim \mathcal{N}(0.4, 0.2), \quad r\eta_{co}^{re} \sim \mathcal{N}(0.7, 0.2), \quad \eta_{v}^{re} \sim \eta_{ci}^{re} + \eta_{co}^{re}. \end{aligned} \tag{56}$$

This means the absolute values of cross-sectional areas of blood vessels follow the Gaussian profiles, where the extra factor r is due to the polar coordinates used. The profiles of volume fractions at steady state are shown in Figure 14(a). The blood supply from boundary is also increased as shown in Table 2, particularly for the Ω_{ai} boundary. The insufficiency of oxygen supply near $r = 1$ is more severe in this case, shown in Figure 14(b).

In the above two cases, we find that (i) the structural profiles of vasculature play essential roles in the overall blood supply and distribution of exchanges, and (ii) although the total blood supply from the boundary is increased with Gaussian cases, the supply of oxygen could still be insufficient in some local region due to the uneven exchanges. To simulate more practi-

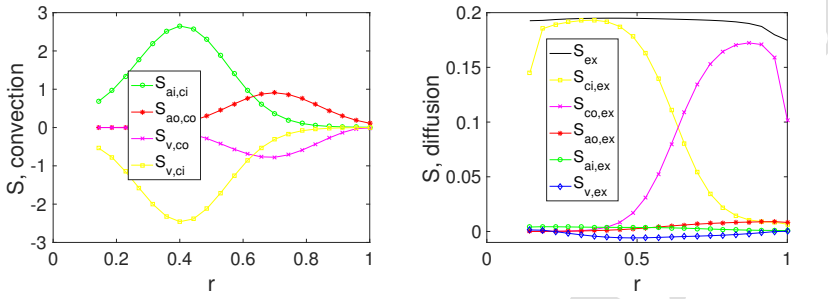

(a) (b)

Figure 13: The oxygen exchange rates in Gaussian case 1.

cal situations, more information on the blood vessel sizes and distributions is needed. Also, the maximum consumption parameter S_{ex}^{max} could vary in space, e.g., depending ion channel/pump distributions, so the distribution of resting capillary volume fractions could help ensure a stable oxygen supply, so important to biological function.

4.2. Effects of leak coefficients

In this subsection, we consider the effects of leak coefficients $L_{j,ex}$ in (7). The changes of these coefficients could be due to the changes of properties of blood vessel walls and could relate to damages from pathological conditions [9, 12, 13]. Since the capillary change/damage could occur more easily, we mainly focus on the coefficients $L_{ci,ex}, L_{co,ex}$ for illustration.

Parameters $L_{ci,ex}, L_{co,ex}$	40 fold	500 fold
% change of Δp_{ai}, Q^*_{ai}	1.5%,1.6%	10.1%,10.7%
% change of Δp_{ao}, Q^*_{ao}	-0.8%, -0.4%	3.6%, 5.9%
% change of Δp_v, Q^*_v	0.5%, 0.6%	7.7%, 8.3%
average $Q_{ci,ex}, Q_{co,ex}$	32 fold	118 fold

Table 3: Changes of pressure drops Δp_j, boundary flow rates Q^*_j $(j = ai, ao, v)$, and average water exchange rates by changing the parameters $L_{ci,ex}, L_{co,ex}$ simultaneously.

For water/blood circulation part, Table 3 and Figure 15 show the changes

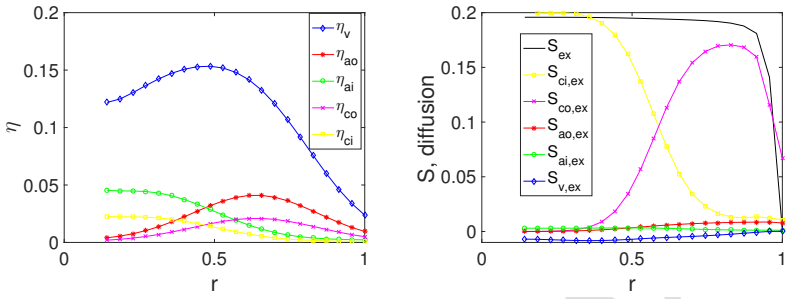

(a) (b)

Figure 14: The profiles of volume fractions and oxygen exchange rates in Gaussian case 2.

of pressure drop and water flow rates produced by gradually increasing $L_{ci,ex}, L_{co,ex}$ simultaneously. We find

- There are more significant changes for pressure drops $\Delta p_k = |p_k(R_0) - p_k(R_1)|$ and boundary fluxes Q_k^* $(k = ai, ao, v)$ after the parameters $L_{ci,ex}, L_{co,ex}$ reach some threshold (e.g., at the value of 10^{-2} μm/(Pa s); about 40 fold of original value), shown in Figure 15(a,b). This is when the water exchange rates $Q_{ci,ex}, Q_{co,ex}$ become comparable with other flow rates between different domains as shown in Figure 15(c,d). For example, Table 3 shows that the boundary flux Q_{ai}^* from CRA increases by 1.6 % with 40 fold parameter increase, but increases by 10.7% with 500 fold parameter increase.

- There is an additional major pathway for water circulation after the threshold

$$\Omega_{ci} \to \Omega_{ex} \to \Omega_{co}, \quad Q_{ci,ex} > 0, \quad Q_{co,ex} < 0, \tag{57}$$

  which is based on the magnitudes and signs of quantities in Figure 15(c,d), e.g, $Q_{ci,ex} > 0, |Q_{ai,ci}| > |Q_{v,ci}|, |Q_{ao,co}| < |Q_{v,co}|$. Table 3 and Figure 15(c) show that there is almost proportional change of $Q_{ci,ex}, Q_{co,ex}$ with respect to the parameter change initially before the threshold, since they are small and unaffected by other flow rates. After the threshold when $Q_{ci,ex}, Q_{co,ex}$ are comparable with other flow rates in Figure 15(d), their changes will interact with other flow rates and

the additional pathway will play important roles on the blood/water circulation.

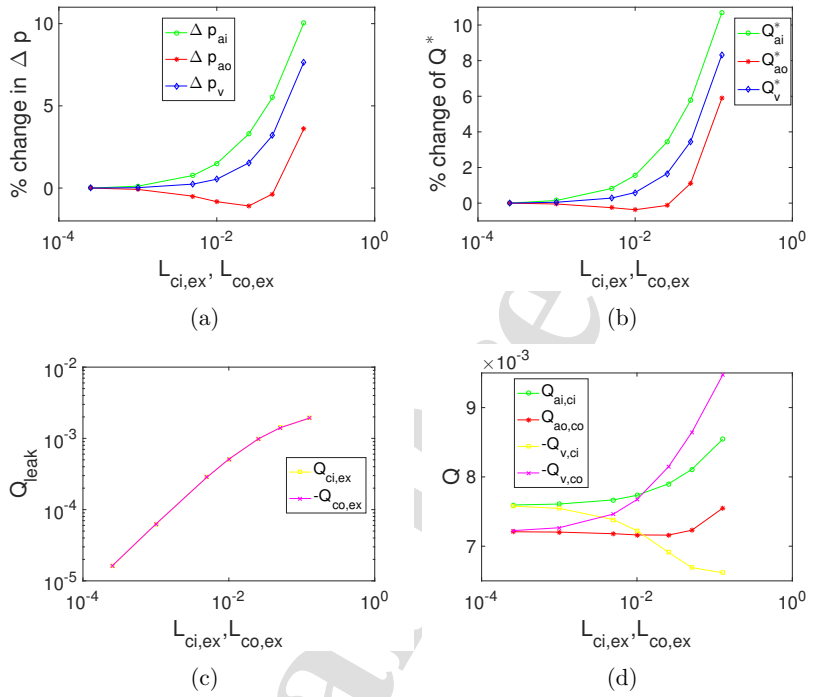

Figure 15: The dependence of pressure drops, boundary flow rates, and average exchange rates on the leak coefficients $L_{ci,ex}, L_{co,ex}$ with unit μm/(Pa s).

For the oxygen transport part, we observe the following:

- Figure 16(a) shows that there are significant increases for the average concentrations C_k $(k = ci, co, ex, v)$ after some threshold for the parameters $L_{ci,ex}, L_{co,ex}$ (e.g., 10^{-2} μm/(Pa s)), which is a consequence of the increased boundary flow rates in Figure 15(b). Figure 16(b) shows that oxygen binding capacity H_{ci} increases and H_{co} decreases significantly after the threshold, as a consequence of the additional pathway of water circulation in (57).

- Figure 17(a) shows that the oxygen consumption is kept at steady level, with less than 0.15% change over the studied range of parameters $L_{ci,ex}, L_{co,ex}$. Figure 17(b) show that the oxygen supply from capillary domain Ω_{ci} increases while that from capillary domain Ω_{co} decreases (so the sum is kept almost constant), as a consequence of the additional pathway of water circulation in (57).

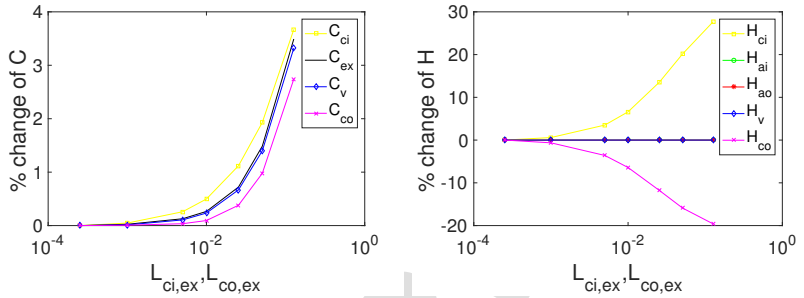

(a) (b)

Figure 16: Percentage changes of average concentrations C_k and average oxygen binding capacities H_k by changing the leak coefficients $L_{ci,ex}, L_{co,ex}$.

In summary, the water leak coefficients through the capillary wall will have strong impacts on blood circulation after they pass a threshold, due to an additional pathway of water circulation. This in turn affects oxygen delivery, with a redistributed supply from the two sets of capillaries.

Remark 2: The effects of leak coefficients $L_{ai,ex}, L_{ao,ex}, L_{v,ex}$ in arteries and veins have very similar features as the above case, except the following differences. With simultaneous changes of these three parameters, the threshold is smaller and at about 10^{-3} μm/(Pa s) since the pressure differences across the blood vessel wall of the artery and vein is larger. The additional pathway for water circulation is

$$\Omega_{ai}, \Omega_{ao} \to \Omega_{ex} \to \Omega_v, \quad Q_{ai,ex} > 0, \quad Q_{ao,ex} > 0, \quad Q_{v,ex} < 0. \tag{58}$$

For the oxygen transport part, the quantities H_k in different domains are affected due to (58).

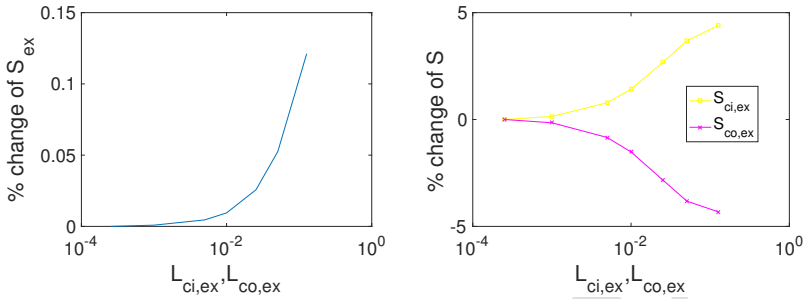

Figure 17: Percentage changes of average oxygen consumption S_{ex} and the oxygen supply from two capillary domains by changing the leak coefficients $L_{ci,ex}, L_{co,ex}$.

4.3. Effects of blood viscosity μ_b

In this subsection, we focus on the effects of blood viscosity μ_b, which could increase due to aging and disease. For the blood/water circulation, by gradually changing μ_b by $\pm 20\%$, we observe that the parameter μ_b has almost a scaling effect for the water/blood flow. The pressure profiles in Section 3.1 stay the same, but all the flow rates change by a factor of $1/\mu$. Figure 18 shows the percentage changes of boundary flow rates Q_k^* $(k = ai, ao, v)$ with changes of μ, which align with the change of $1/\mu_b$ for illustration of scaling effect. This scaling effect can also be seen from the governing equations and parameter relations.

For the oxygen transport, Figure 19(a) shows that the average concentrations for C_j $(j = ci, co, v, ex)$ over the region decrease as μ increase, for example, they decrease by 6-8% with μ increased by 20 %. The decrease is a consequence of decreased blood supply in Figure 18. But the difference between the capillary concentrations and extravascular concentrations is relatively stable, so the oxygen exchanges from the two capillaries to the extravascular space only drops slightly ($< 1\%$ with μ increased by 20 %), as shown in Figure 19(b). The total consumption is also kept relatively stable in Figure 19(b), computed with the uniform case for resting volume fractions.

Remark 3: The average S_{ex} is decreased from 0.192 to 0.189 compared with the values in Figure 13(b), computed with the Gaussian case 1 and when μ

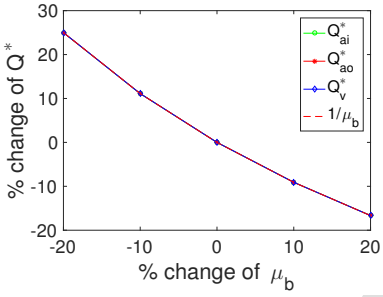

Figure 18: Percentage change of boundary blood supply with changing μ.

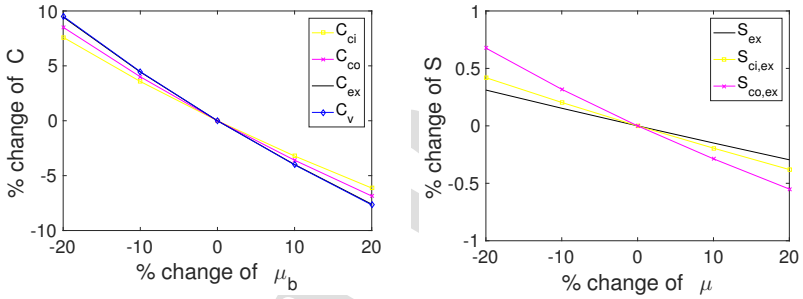

(a) (b)

Figure 19: oxygen with changing μ

increased by 20 %. In addition, S_{ex} is impacted significantly locally near $r = 1$, decreasing from 0.175 in to 0.146. This decrease is expected since less boundary blood supply will have more severe effects on the local region with limited vasculature.

Next, we investigate how much the pressure at the artery boundary should be adjusted to maintain the normal blood supply when μ increases. At the boundary, fixed flow rates Q^*_{ai}, Q^*_{ao} in (44) are used to replace the pressure boundary conditions, and they are set to be the same as the reference case. Table 4 shows the pressure adjustments at the artery boundary needed to maintain blood supply with increase of μ. Pressures have to increase by 8.2%

(3.3 mmHg) for $P_{ai,0}$ and by 6.5% (2 mmHg) for $P_{ao,1}$ when μ is increased by 20%. In the uniform case, the oxygen delivery is not affected much, but for the Gaussian cases the oxygen supply in local regions will be affected.

In summary, increased viscosity has a scaling effect on blood circulation decreasing according to the factor $1/\mu_b$. The decreasing blood circulation in turn affects the oxygen concentrations. It could worsen the local oxygen delivery for non-uniform cases. Biologically, the blood pressure in the artery has to increase correspondingly when μ is increased under various conditions, in order to provide sufficient blood supply and oxygen delivery.

increase of μ	0	10%	20%
$P_{ai,0}$	2	2.0834, (4.2%, 1.7 mmHg),	2.1648, (8.2%, 3.3 mmHg)
$P_{ao,1}$	1.5	1.5488, (3.3%, 1 mmHg)	1.5974, (6.5%, 2 mmHg)

Table 4: Pressure adjustments at artery boundary to maintain blood supply with an increase of μ.

4.4. Effects of pulsatile arterial pressure

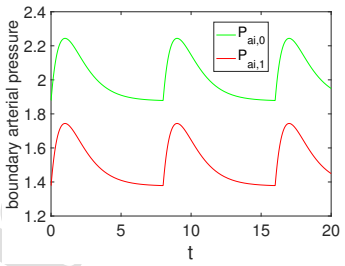

Figure 20: Pulsatile profiles of boundary arterial pressures for $P_{ai,0}, P_{ao,1}$.

The pressure in arteries varies periodically as the heart beats so we consider the case of pulsatile changes of arterial pressure. Figure 20 shows the pulsatile profiles of the dimensionless boundary arterial pressures $P_{ai,0}(t)$ and $P_{ao,1}(t)$ in (12,14) used as boundary conditions of the following simulation. The profile of variation is constructed roughly based on a shifted function $t * e^{-t}$ in the first period, which has a shape similar to a pulse profile. The

period is T=8, which is 0.8 seconds with units. The total variation within one period is about 0.365, i.e., the pulse pressure between the systolic and diastolic pressures is about 7.3 mmHg with units. The dimensionless average values (mean arterial pressures, MAP) for $P_{ai,0}, P_{ao,1}$ over one period are the same as the reference values 2 and 1.5 (i.e., 40 mmHg and 30 mmHg with units), which are located at 1/3 of total variation and therefore consistent with the common definition. For illustration, we chose our curves in Figure 20 based on profiles of pressures and flow rates in [26, 44, 45, 46, 47, 43] and the knowledge of MAP in [28, 6, 47]. More specific references may be available for more accurate curves that we have not yet found in the dauntingly large experimental literature.

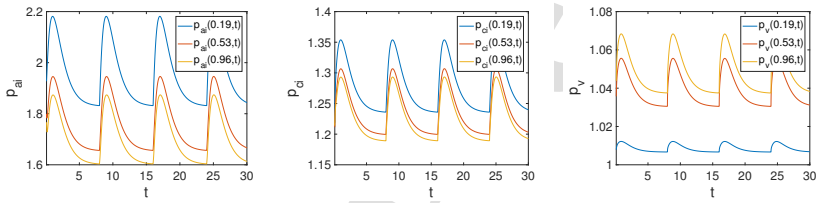

(a) (b) (c)

Figure 21: dynamics of the three pressures p_{ai}, p_{ci}, p_v at three locations $r = 0.19, 0.53, 0.96$.

Figure 21 shows the dynamics of the three pressures p_{ai}, p_{ci}, p_v at three typical locations $r = 0.19, 0.53, 0.96$ (one in the middle, two close to two ends). They all show pulsatile oscillations similar to the profile shown in Figure 20, but with different magnitudes of variations. The pulsatile variations in arteries are the largest in magnitude, and the variations in veins are the smallest. The other pressures show similar trend and variations. The volume fractions show small pulsatile changes due to the force balance and changes in pressure.

Figure 22 shows the spatial profiles of all pressures in the whole region at two particular times when the boundary arterial pressures are maximum and minimum (systolic and diastolic pressures respectively). The spatial profiles and their relative positions for pressures are quite similar to those in Figure 3, but move up and down simultaneously and stably according to dynamic changes in boundary arterial pressures shown in Figure 20.

Figure 23 shows the dynamics of the boundary blood flow rates, which

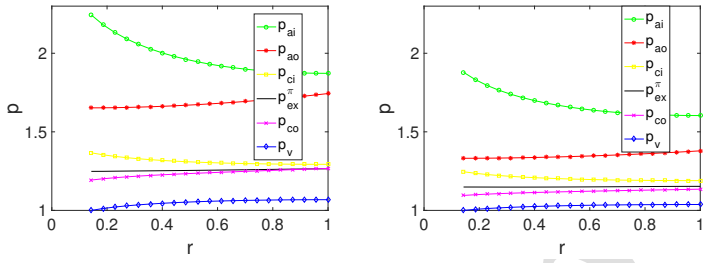

Figure 22: spatial profiles of all pressures in the whole region at two particular times (i.e., systolic and diastolic pressures respectively).

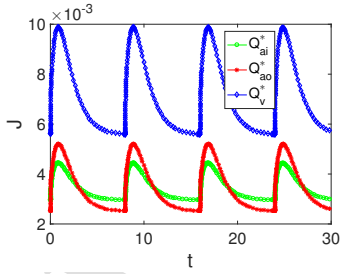

Figure 23: The dynamics of the boundary blood flow rates in the pulsatile case.

have a similar pulsatile profile to the given boundary arterial pressures. The average value of blood flow rates over one period is computed to be $Q^*_{ai} = Q^*_{ao} = 0.0034$, the same as those in Table 2 with uniform case. So for the blood circulation, the uniform case in Section 3.1 can be considered as the averaged version of the case with pulsatile arterial pressure. In nonlinear time dependent systems of complex structure, the average of the output variable must be computed.

Figure 24 shows the dynamics of the concentrations and oxygen consumption at $r = 0.53$. The concentrations show pulsatile variations but the total oxygen consumption is relatively stable with very small variation. The small variation for oxygen consumption is due to the relation $S_{ex}(C_{ex})$ used in Figure 6, because even with changes of C_{ex}, say in [0.4,0.5], the consumption

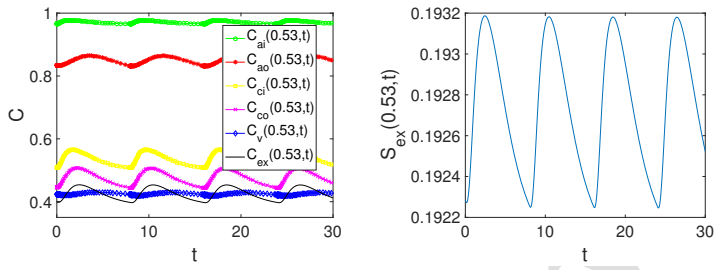

(a) (b)

Figure 24: The dynamics of the concentrations and oxygen consumption at $r = 0.53$.

S_{ex} stays at almost stable constant level. Then, as a consequence of stable consumption in Figure 24(b) and varying (but sufficient) flow rates in Figure 23, the concentrations will have more significant variations, i.e., with more blood flow (and RBCs) from boundary, the concentrations do not need to drop too much to provide and allow stable oxygen consumption. We also notice there is a delay in the timing of peak values of concentrations compared with the timing of peak values of blood flow rates (i.e., the timing of systolic pressure).

In summary, with pulsatile pressure conditions, the blood circulation and oxygen concentrations show similar pulsatile variations in time and stable spatial profiles. The uniform case is almost the averaged version of pulsatile case despite the evident complex time dependent nonlinear system involved. The simple behavior of averaged quantities, compared to what might happen in such complex systems, may help the animal control the systems involved in a stable reproducible way.

4.5. Effects of other parameters

In this subsection, we study the effects of a few other model parameters, including $\lambda_j, \beta_j, \delta_j$ in blood circulation part and $S_{ex}^{max}, C_{1/2}, C_{ai,0}, H_0$ in the oxygen delivery part.

First, we study the effects of the modulus λ_j ($j = ai, ao, v, ci, co$) of the blood vessel wall in the force balance of equation (11). The diameters of blood vessels might change in response to the physiological changes (or stimulus like oxygen) [6, 16, 23]. In our models, this could come from the response of blood vessel wall property to the physiological changes. For example, in

the present framework, the feedback effect of oxygen on blood flow could appear in the model as the dependence of λ_j on oxygen concentrations. Here, we illustrate the effect of λ_j $(j = ai, ao, v, ci, co)$ by reducing all the moduli λ_j simultaneously. Table 5 shows the comparison of the reference uniform case and the case when all λ_j are reduced by 50%, showing that the volume fractions for η_j, particularly for η_{ai}, η_{ci}, are increased, which in turn increases the blood supply from the boundary, particularly for Q^*_{ai}. The main reason for the increase in blood supply is the change in permeabilities between vascular domains $\bar{\kappa}_j, \bar{K}_j$ in (41). The permeabilities increase with the increased volume fractions (or diameters of blood vessels), leading to more blood flow. The influence on oxygen delivery is not as significant, since in the uniform case, the blood supply and oxygen supply is quite sufficient and stable: the increased blood flow is not needed to help out. We also tested the Gaussian case 1, when all λ_j are increased by 50%, the minimum value of S_{ex} near $r = 1$ in Figure 13(b) increases from 0.1748 to 0.1794, so in that case the change of λ_j can help the local oxygen delivery.

Remark 4: The parameter λ_j could depend on many factors, including the Young's modulus, thickness of blood vessel wall, and the reference/prestress states in mechanical models, see [26]. Some models for the modulus λ_j (or effective tensions) include the details of smooth muscle cells, e.g., the chemical states or the smooth muscle tone, through introduction of an activation parameter [6, 23, 22]. The activation parameter then depends on the changes of physiological conditions, such as oxygen concentration, release of ATP, the incoming blood pressures etc. We will leave the detailed description of λ_j to future work. Here we only briefly mention that a simple model for autoregulation [16] assumes that the resistance in blood vessels increases with venous oxygen concentration. In the context of the present model, we can assume the modulus λ_j increases with tissue oxygen concentration C_{ex}. In that case, smaller oxygen supply (smaller C_{ex}) means smaller λ_j and larger volume fractions η_j (larger diameter of blood vessels) by (11) and consequently larger permeability κ_k in (3).

Next, we analyze the effects of partial blockage of blood vessels in some local regions in either artery or capillary, which could be caused by pathological conditions such as arterial stenosis [26, 6]. The blockage leads to decreased permeability, and for illustration, we take β_{ai} and δ_{ci} as the effective parameter for the blockage of artery and capillary. In Figure 25, we set

	η_{ai}	η_{ao}	η_{ci}	η_{co}	Q^*_{ai}	Q^*_{ao}
with λ_j in Uniform case	0.0143	0.0257	0.0070	0.0131	0.0034	0.0034
reduce λ_j by 50%	0.0160	0.0262	0.0077	0.0135	0.0042	0.0035

Table 5: Effects of λ_j in the uniform case.

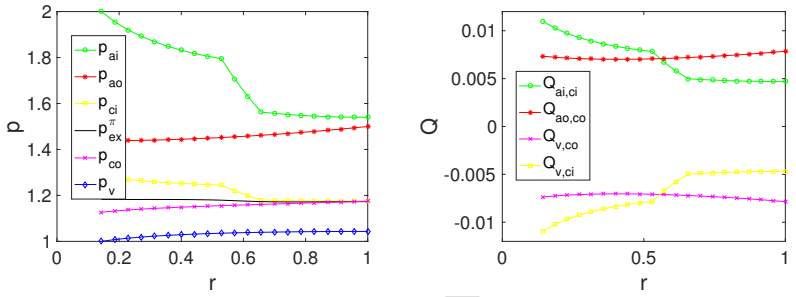

(a) (b)

Figure 25: Pressure profiles and blood exchange rates with local change of β_{ai}, which is reduced to 10% of original value near $r = 0.6$.

β_{ai} to be 10% of original value (i.e., 90% decrease) in a small interval near $r = 0.6$, more precisely in $r = [0.52, 0.62]$. Figure 25(a) shows that the pressures p_{ai} and p_{ci} have a more significant drop near $r = 0.6$ to counterbalance some blockage effect. The average value of blood flow rates $Q_{ai,ci}$ and $Q_{v,ci}$ downstream from the locations of blockage are reduced by 26% (from 0.0065 to 0.0048), shown in Figure 25(b). The boundary input Q^*_{ai} is reduced by 15% (from normal value 0.0034 to 0.0029). For the oxygen delivery part, the overall oxygen delivery/consumption is still quite stable without observable change, since the overall blood supply is still sufficient and there is redistribution of oxygen supply in the affected region. More supply comes from the other capillary domain Ω_{co}. We have also tested the case when β_{ai} is reduced by 50% locally, and the changes for $Q_{ai,ci}, Q_{v,ci}$ and Q^*_{ai} are quite small ($< 3\%$ decrease).

In Figure 26, we set δ_{ai} to be 10% of original value in a small interval $r = [0.52, 0.62]$ with other region unchanged. In Figure 26 (a), the flow rates $Q_{ai,ci}$ and $Q_{v,ci}$ are reduced by about 80% (from 0.0071 to 0.0015) locally in that

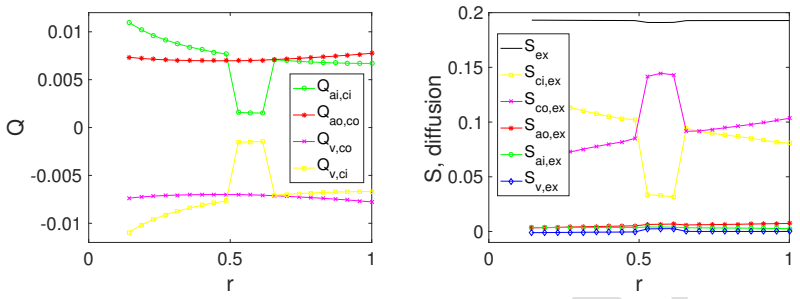

(a) (b)

Figure 26: Blood exchange rates and oxygen supply with local change of δ_{ci}, which is reduced to 10% of original value near $r = 0.6$.

modified region $r = [0.52, 0.62]$, while other regions are almost unaffected. This is because the local change in δ_{ai} only affects the local exchange between capillary domain Ω_{ci} and the corresponding artery and vein domains Ω_{ai}, Ω_v through the effective conductance in (8,9). There are no in-domain flows in capillary since they are not directly connected in different locations, and the other capillary network related to Ω_{co} is a separate network and hence $Q_{ao,co}$ and $Q_{v,co}$ are unaffected. In Figure 26 (b), only significant changes for $S_{ci,ex}, S_{co,ex}$ are observed in the local modified region $r = [0.52, 0.62]$, as a consequence of local changes of blood supply. But overall, the oxygen consumption only drops slightly (about 1%) , since it is compensated by more oxygen supply from the undamaged capillary Ω_{co}. We have also tested the case when both δ_{ci} and δ_{co} are reduced by 90%, the reduction in flow rates are similar and at about 80%, but the oxygen consumption only drops by about 8.4% mainly due to the relation $S_{ex}(C_{ex})$.

In brief, the system is not very sensitive to permeability changes mainly because of the presence of two capillary networks and the relation $S_{ex}(C_{ex})$ with small $C_{1/2}$ in Figure 6(b).

Next, we analyze the effects on oxygen consumption of the parameters S_{ex}^{max} and $C_{1/2}$ in the Michaelis-Menten formula (25). Due to lack of data, these two parameters are estimated based on different tissues in Appendix A.2 [25, 24, 18] and the simulated results for oxygen concentrations, so they do not necessarily reflect the real situation for the optic nerve. These param-

eters are biologically important, for example, the max demand S_{ex}^{max} could change because of high metabolism or neuron activities. We examine a case when S_{ex}^{max} is increased by 50%. The first two rows in Table 6 show, for the uniform case, that the consumption of oxygen also increases correspondingly by roughly 50% on average and keeps stable spatial profile, but the concentrations C_{ex}, C_v are decreased accordingly as more oxygen from RBCs has to release to meet the increased need. For Gaussian case 1, the last two rows in Table 6 show similar increased average consumption and decreased average concentrations C_{ex}, C_v. But locally near $r = 1$, the minimum oxygen consumption is affected significantly and reduced to 13% of average value, since the mismatch between demand and supply is worsened: the blood supply is insufficient there. The parameter $C_{1/2}$ influences the shape of the consumption curve in Figure 6(b). With increased $C_{1/2}$ the curve will have a smoother transition and lie below the original curve. So with increased $C_{1/2}$, the average consumption will be smaller for uniform case, and more local regions will be affected for oxygen delivery in the Gaussian case 1 due to insufficient blood supply and more sensitive changes of S_{ex} with C_{ex} in certain range (say [0.2, 0.4]).

In brief, increased S_{ex}^{max} or $C_{1/2}$ will worsen the oxygen supply for local regions with insufficient blood supply.

	average C_{ex}	average C_v	average S_{ex}	min S_{ex}
reference Uniform case	0.424	0.429	0.193	0.193
increase S_{ex}^{max} by 50%	0.357	0.351	0.287	0.287
reference Gaussian case 1	0.456	0.378	0.192	0.175
increase S_{ex}^{max} by 50%	0.379	0.308	0.272	0.035

Table 6: Effects of S_{ex}^{max} by increasing it by 50%.

Finally, we study the effects of parameters $C_{ai,0}$ (we set $C_{ai,0} = C_{ao,1}$) and H_0 in (35,36), which are related to the supply of oxygen from the artery boundary. Biologically, the oxygen content from the boundary artery could drop due to various conditions like anemia (i.e, low H_0) and high altitude or carbon monoxide poisoning (i.e., low $C_{ai,0}$). For the uniform case, when H_0 or $C_{ai,0}$ is decreased by 20%, there is only negligible impact on the oxygen delivery, e.g., the consumption rate S_{ex} has negligible change (deceased by $< 1\%$), because the supply of blood flow and hence oxygen is still sufficient.

For the Gaussian case 1, Table 7 shows the comparison when the $C_{ai,0}$ or H_0 is decreased by 20%. With $C_{ai,0}$ decreased by 20%, the profile and values of S_{ex} have negligible change ($< 1\%$ for mean and minimum values), while the concentrations decrease by moderate percentage (e.g., 5-7%). That means the overall profiles of concentrations are shifted downward to maintain relatively stable oxygen consumption. With H_0 decreased by 20%, the oxygen consumption/supply in some local region will be affected more significantly, as the minimum S_{ex} drops from 0.175 to 0.146 near $r = 1$. This is because the oxygen in hemoglobin (in RBCs) is the main source of oxygen supply, and if hemoglobin concentration is decreased (here reflected by H_0), the supply of oxygen is worsened in local regions with insufficient blood supply. The concentrations like C_{ex}, C_v will be decreased accordingly (by about 10%) since this allows more oxygen release from hemoglobin to maintain roughly stable S_{ex}. Overall, decreased H_0 has more impact on local regions compared to decreased $C_{ai,0}$.

	average C_{ex}	average C_v	average S_{ex}	min S_{ex}
reference Gaussian case 1	0.456	0.378	0.192	0.175
decrease $C_{ai,0}$ by 20%	0.421	0.359	0.191	0.172
decrease H_0 by 20%	0.414	0.339	0.189	0.146

Table 7: Effects of H_0 and $C_{ai,0}$ in the Gaussian case 1.

5. Conclusions

In this work, we have developed a multi-domain model for blood circulation and oxygen transport in the optic nerve, with biological structures and various physical mechanisms incorporated. The arteries, veins and capillaries of the vasculature are treated as different domains in the model for the same geometric region. Simulated baseline results show mechanisms and scales consistent with literature and intuition. Then, the effects of various important model parameters (relevant to pathological conditions) are investigated in detail, and the model provide insights into the possible implications from those parameter changes.

Vasculature distribution (represented by resting volume fractions here) has significant impact on blood flow and oxygen transport. With uniform distributions, we find that the blood flow is sufficient and oxygen delivery is quite

stable and not sensitive to many parameter changes. With non-uniform distribution like Gaussian profiles, the flood flow and oxygen transport changes drastically, e.g., leading to limited oxygen supply locally. **Therefore, the biological structural data for vasculature distribution (volume fractions) is crucially important to make accurate predictions.**

Some existing models have also attempted to generate vasculature based on branching processes in simulations. Once the biological data are available, they can be incorporated.

We also comment that we have included two complete sets of vasculature with artery, capillary and vein for the optic nerve, while some existing models may have only concentrated on the artery or capillary. For tissues with one set of vasculature, the five vascular domains here will be simplified to three domains.

The effects of leak coefficients, particularly for the capillary, are investigated, showing that blood circulation and hence oxygen supply will be strongly affected. The change of leak coefficients are related to damages in optic nerve due to pathological conditions, such as glaucoma and diabetic retinopathy. More work is needed in the future to make connections between these parameters and diseased states.

We have investigated the effects of blood viscosity and incoming artery pressures. The viscosity affects blood circulation through a scaling factor. When viscosity is increased due to aging or other physiological conditions, the incoming blood pressure in the artery has to increase to maintain original blood circulation.

The case which mimics the natural heart beat is also investigated. Pulsatile incoming (boundary) artery pressure produces similar averaged quantities for blood circulation as in the constant pressure case. But one of our paper's limitations is that the changes of blood vessel modulus have not yet been incorporated into the dynamics of the natural beating, pulsatile case.

We have studied the sensitivity of results to other model parameters including modulus, permeability, maximum oxygen consumption rate, oxygen content supply from the boundary, etc., through variations by a certain percentage. We note that the feedback effect of oxygen on blood circulation could be modeled through modulus changes in future models. The estimate of maximum oxygen consumption rate is also important and needs more biological data.

There are other possible generalizations from this framework. This work focuses on a 1D case based on the optic nerve geometry and simplicity con-

siderations, but it can be extended to high-dimensional cases (e.g., in (r, z) space) when more biological structural information is available. Some existing multi-domain models on optic nerve have focused on the ion transport and water flow in the tissue domain (with subdomains), and the modeling of vasculature with multi-domains here can be combined with those models so that the physical coupling mechanisms for water flow, ion transport, oxygen transport etc. can be studied together. We also hope to extend this framework to the retina, where more image/experimental data are available.

The multidomain model of oxygen transport in the optic nerve has been investigated in great detail for a specific reason. The possibility exists that many diseases of great interest are the result of prolonged deprivation of oxygen. Our work seeks to understand the processes that control oxygen deprivation, for that reason.

We show that many changes in parameters can cause oxygen deprivation. The confusing clinical picture of such diseases as glaucoma may arise because there are many ways to deprive tissues of oxygen, as we show here. Perhaps each of them leads to a similar final clinical picture, e.g. end stage glaucoma. We believe that a combination of modelling and experimentation will be needed to separate the different kinds of glaucoma (for example) produced by different changes in parameters and thus to lead to appropriate treatments for each kind.

Appendix A. Parameter values and estimates

Appendix A.1. Parameters in blood/water circulation

Appendix A.1.1. Estimate of β_j and $M^0_{j,ex}$

First, we estimate the values of β_k $(k = ai, ao, v)$ in (3), and we omit the subscript k in some derivation below. In Poiseuille's flow through a cylindrical blood vessel of radius r_{bv}, the permeability κ (the κ_j in the formula of (2)) is derived as [15, 16]

$$\kappa = \frac{1}{8} r_{bv}^2.$$

The volume fraction η is given by [15]

$$\eta = \pi r_{bv}^2 N_{bv} L/V,$$

Table A.8: The parameters in blood circulation

parameter	value	references
Radius of central vessels R_0	113 μm	[15]
Radius of the optic nerve R_1	790 μm	[15]
Tissue/Extravascular pressure $P_{ex,1}$	2.92 mmHg	[15]
CRA pressure $P_{ai,0}$	40 mmHg	[15]
PCA pressure $P_{ao,1}$	30 mmHg	[15]
CRV pressure $P_{v,0}$	20 mmHg	[15]
osmotic pressure constant π_{ex}	8 mmHg	[16]
osmotic pressure constant π_j in vessel	28 mmHg	[16]
vascular volume fraction $\sum \eta_k^{re}$	15.67 %	[15]
capillary, averaged $\eta_{co}^{re} + \eta_{ci}^{re}$	1.9 % =1.27+ 0.63 %	[48]
volume fraction, average η_v^{re}	10 %	[15, 16]
volume fraction, average $\eta_{ao}^{re} + \eta_{ai}^{re}$	3.77 %= 2.51+1.26 %	[15, 16]
area coefficient $M_{v,ex}^0$	0.021 $/\mu m$	estimate
area coefficient $M_{ao,ex}^0$	0.016 $/\mu m$	estimate
area coefficient $M_{ai,ex}^0$	0.011 $/\mu m$	estimate
area coefficient $M_{co,ex}^0$	0.075 $/\mu m$	estimate
area coefficient $M_{ci,ex}^0$	0.053 $/\mu m$	estimate
permeability coefficient β_v	9000 $(\mu m)^2$	estimate
permeability coefficient β_{ao}	16000 $(\mu m)^2$	estimate
permeability coefficient β_{ai}	31500 $(\mu m)^2$	estimate
permeability κ_{ex}	$4 \times 10^{-4} (\mu m)^2$	[3]
tortuosity τ_{ex}	0.9	estimate
tortuosity $\tau_{ai}, \tau_{ao}, \tau_v$	0.5	estimate
leak coefficient $L_{ao,ex}, L_{ai,ex}, L_{v,ex}$	1×10^{-6} μm/(Pa s)	[3]
water leak coefficient $L_{ci,ex}, L_{co,ex}$	2.54×10^{-4} μm/(Pa s)	[39]
permeability coefficient δ_{ai}	0.39 /(Pa s)	estimate
permeability coefficient δ_{ao}	0.2 /(Pa s)	estimate
permeability coefficient δ_v	0.11 /(Pa s)	estimate
permeability coefficient δ_{ci}, δ_{co}	3.25, 1.61 /(Pa s)	[48]
viscosity μ_b, μ_{ex}	0.011 Pa s	[15, 25, 49]
modulus $\lambda_j, j = ai, ao, ci, co$	7.8×10^5 Pa	[15]
modulus λ_v	1.5×10^5 Pa	estimate
resting pressure P_{ex}^{re}	2.92 mmHg	estimate
resting pressure P_{ai}^{re}, P_{ao}^{re}	25 mmHg	estimate
resting pressure $P_v^{re}, P_{ci}^{re}, P_{co}^{re}$	20 mmHg	estimate

where V is a control volume, L and N_{bv} are the length and number of parallel blood vessels in the control volume. So, we can write them as

$$r_{bv}^2 = \beta\eta, \quad \beta = \frac{V}{\pi N_{bv} L}, \quad \kappa = \frac{1}{8}\beta\eta,$$

where the last one is the formula (3) used in the maintext, and the first formula will be used to estimate the coefficient β. Here we assume constant β for simplicity (of course, β could be varying as it characterizes the structural information about distribution of branches) and estimate it by choosing an average radius of blood vessel for each domain. For example, we choose average $r_{bv} = 30\mu m$ for vein domain and get

$$\beta_v \approx \frac{r_{bv}^2}{\eta_v^{re}} = \frac{(30\mu m)^2}{0.1} = 9000(\mu m)^2.$$

Similarly we choose $r_{bv} = 20\mu m$ for two artery domains and get β_{ai}, β_{ao} respectively as in Table A.8. We also choose $r_{bv} = 3\mu m$ for capillary domains to get β_{ci}, β_{co} (although not directly used in maintext), which will be used to estimate $M^0_{ci,ex}, \delta_{ci}, M^0_{co,ex}, \delta_{co}$.

Next, we estimate $M^0_{j,ex}$ defined in (6), and omit j, ex in the general formula below. By definition, the area of blood vessel wall per unit control volume is

$$M = 2\pi r_{bv} N_{bv} L/V = 2\sqrt{1/\beta}\sqrt{\eta} = M^0\sqrt{\eta} \quad \Rightarrow \quad M^0 = 2\sqrt{1/\beta},$$

where the definitions of η, β are used in the second equality. Then, for each domain, we have the estimate

$$M^0_{j,ex} = 2\sqrt{1/\beta_j}, \quad j = ai, ao, v, ci, co.$$

Appendix A.1.2. Estimate of δ_j

The estimate of δ_j is also based on β_j. For example, δ_{ai} is estimated as

$$\delta_{ai} = \frac{1}{8}\frac{\beta_{ai}\tau_{ai}}{\mu_b}\frac{1}{(\Delta r)^2} \approx 0.39/(\mathrm{Pa\,s})$$

where $\Delta r = R_1 - R_0 = 677\mu m$ is used. Similarly the same Δr is used for estimates of δ_{ao}, δ_v. For capillary domains, we have used $\Delta r = 50\mu m$ to estimate δ_{ci}, δ_{co}, because capillary network is local and connects the artery and vein domains. The estimated δ_{ci}, δ_{co} have similar values as those calculated from [48].

Appendix A.1.3. Other estimates

The total resting volume fractions for two arteries are taken from [15, 16]. We split it as two parts, 2/3 for the domain Ω_{ao} and 1/3 for the domain Ω_{ai}, because it is believed that the artery from PCA is the primary component [15, 35]. Similarly, we adopted the split the total capillary resting volume fraction (from [48]) as two parts, 2/3 and 1/3 respectively for the two capillary domains Ω_{co}, Ω_{ci}. The modulus λ_j for arteries are taken from [15] (see also [43, 40]), and the λ_v is chosen to be 5 times smaller than that, because the compliance (related to the inverse of $\lambda_j \eta_j$ here) is about 24 times larger in veins [16]. The tortuosity in blood vessels are chosen as 0.5 because this is related to the relative orientation/angle of blood vessels to the radial direction, while it is set as 0.9 for extracellular space since it is almost connected in every direction.

Appendix A.2. Parameters in oxygen transport

Since we directly used the concentration of oxygen instead of partial pressure of oxygen in our model, the values from the following references will be converted by multiplying oxygen solubility coefficient α_{O2}. After conversion, the max consumption rate S_{ex}^{max} is $6 * 10^{-4}$ ml O2/ml/s in [25] for retina, and some consumption rate in the range $[1, 42] * 10^{-4}$ ml O2/ml/s is used in [24], the value $23 * 10^{-4}$ ml O2/ml/s is used in [18] for the brain. Based on some simulation, in order to be compatible with estimates of blood flow velocity and normal oxygen concentrations (about 40 mmHg partial pressure multiplied by α_{O2}) in vein, we choose a relatively larger one $6 * 10^{-3}$ ml O2/ml/s for the the parameter S_{ex}^{max} in optic nerve. The values of $C_{1/2}, C_{50}$ etc are taken from [25] after conversion. Many other parameters in Table A.9 are also taken from [25] except C_{Hb}, H_0, because their parameters (a factor of 0.45 is double counted there) are inconsistent with other references [7, 24].

The permeability of oxygen in capillary is estimated by the formula [25]

$$l_{ci,ex} = l_{co,ex} = \frac{D_w}{t_{cap}} = \frac{1 * 10^{-9} \mathrm{m}^2/\mathrm{s}}{0.5 \mu \mathrm{m}} = 0.002 \mathrm{m/s}$$

where D_w is the diffusivity and t_{cap} is the thickness for capillary vessel wall. The values are similar to those in [20]. For artery and vein, we used the same formula, but with a much smaller diffusion constant and a larger vessel wall thickness [42]

$$l_{ai,ex} = l_{ao,ex} = l_{v,ex} = \frac{D_w}{t_{ai}} = \frac{1 * 10^{-10} \mathrm{m}^2/\mathrm{s}}{2 \mu \mathrm{m}} = 5 * 10^{-5} \mathrm{m/s}.$$

Table A.9: Parameters in oxygen transport

max consumption rate S_{ex}^{max}	6×10^{-3} ml O2/ml/s	estimate
half-max parameter $C_{1/2}$	4.8×10^{-5} ml O2/ml	[25]
solubility coefficient in blood α_{O2}	3×10^{-5} ml O2/ml /mmHg	[25]
boundary concentration $C_{ai,0}, C_{ao,1}$	3×10^{-3} ml O2/ml	[25]
average concentration of $[Hb]$ in blood	0.15 g/ ml	[7, 19]
binding-capability of Hb, C_{Hb}	1.34 ml O2/g	[7]
average binding-capability of blood, H_0	0.2 ml O2/ml	[7, 24]
Hill exponent n_{Hill}	2.7	[25]
Half saturation constant in Hb, C_{50}	8×10^{-4} ml O2/ml	[25]
diffusion constant $D_k, k = ai, ao, v, ci, co$	2.18×10^{-9} m^2/s	[25]
diffusion constant D_{ex}	1×10^{-9} m^2/s	[25]
oxygen permeability, $l_{ci,ex}, l_{co,ex}$	0.002 m/s	[25]
oxygen permeability, $l_{ai,ex}, l_{ao,ex}, l_{v,ex}$	5×10^{-5} m/s	[25]
diffusion constant $D_{ai,ci}, D_{ao,co}$	3.6×10^{-5} /s,7.3×10^{-5} /s	estimate
diffusion constant $D_{v,ci}, D_{v,co}$	2.8×10^{-4} /s	estimate

For the estimates, we also referred to [18].

For the effective diffusion constants between vascular domains, we take $D_{ai,ci}$ for example, which is estimated by harmonic average

$$D_{ai,ci} = \frac{D_{ai}^* D_{ci}^*}{D_{ai}^* + D_{ci}^*} \approx 3.6 * 10^{-5}/s$$

where

$$D_{ai}^* = \frac{\eta_{ai} D_{ai} \tilde{\tau}_{ai}}{(\Delta r)^2} \approx 3.6 * 10^{-5}, \quad D_{ci}^* = \frac{\eta_{ci} D_{ci} \tilde{\tau}_{ci}}{(\Delta \tilde{r})^2} \approx 3.3 * 10^{-3}$$

where $\Delta r = 667\mu$m and $\Delta \tilde{r} = 50\mu$m are used for artery and capillary. The other three $D_{ao,co}, D_{v,ci}, D_{v,co}$ are estimated similarly.

Acknowledgments

This work was partially supported by the National Natural Science Foundation of China (grant numbers 12231004, 12071190).

References

[1] X. Cao, Z. Song, T.-L. Horng, H. Huang, Electric potential generation of electrocytes: Modelling, analysis, and computation, Journal of Theoretical Biology 487 (2020) 110107.

[2] Z. Song, X. Cao, T.-L. Horng, H. Huang, Electric discharge of electrocytes: Modelling, analysis and simulation, Journal of Theoretical Biology 498 (2020) 110294.

[3] Y. Zhu, S. Xu, R. S. Eisenberg, H. Huang, Optic nerve microcirculation: Fluid flow and electrodiffusion, Physics of Fluids 33 (4) (2021).

[4] Y. Zhu, S. Xu, R. S. Eisenberg, H. Huang, A bidomain model for lens microcirculation, Biophysical journal 116 (6) (2019) 1171–1184.

[5] R. Eisenberg, Structural analysis of fluid flow in complex biological systems (2022).

[6] G. Guidoboni, A. Harris, R. Sacco, Ocular fluid dynamics: anatomy, physiology, Imaging Techniques, and Mathematical Modeling, Springer, 2019.

[7] R. N. Pittman, Regulation of tissue oxygenation (2016).

[8] B. Hille, Ion channels of excitable membranes, Sinauer Associates, Inc., 2001.

[9] N. Moyseyenko, Disorders of aqueous humor flow in the posterior part of the eye in the mechanisms of optic nerve damage development (literature review)., Journal of Ophthalmology (Ukraine)/Oftal?mologičeskij Žurnal (5) (2023).

[10] E. Ivanova, T. Kovacs-Oller, B. T. Sagdullaev, Vascular pericyte impairment and connexin43 gap junction deficit contribute to vasomotor decline in diabetic retinopathy, Journal of Neuroscience 37 (32) (2017) 7580–7594.

[11] A. L. Gerber, A. Harris, B. Siesky, E. Lee, T. J. Schaab, A. Huck, A. Amireskandari, Vascular dysfunction in diabetes and glaucoma: a complex relationship reviewed, Journal of glaucoma 24 (6) (2015) 474–479.

[12] T. D. Lamb, S. P. Collin, E. N. Pugh Jr, Evolution of the vertebrate eye: opsins, photoreceptors, retina and eye cup, Nature Reviews Neuroscience 8 (12) (2007) 960–976.

[13] G. Guidoboni, R. Sacco, M. Szopos, L. Sala, A. C. Verticchio Vercellin, B. Siesky, A. Harris, Neurodegenerative disorders of the eye and of the brain: a perspective on their fluid-dynamical connections and the potential of mechanism-driven modeling, Frontiers in Neuroscience 14 (2020) 566428.

[14] Y. Wang, A. Lu, J. Gil-Flamer, O. Tan, J. A. Izatt, D. Huang, Measurement of total blood flow in the normal human retina using doppler fourier-domain optical coherence tomography, British Journal of Ophthalmology 93 (5) (2009) 634–637.

[15] D. Prada, A hybridizable discontinuous Galerkin method for nonlinear porous media viscoelasticity with applications in ophthalmology, Purdue University, 2016.

[16] J. Keener, J. Sneyd, Mathematical physiology: II: Systems physiology, Springer, 2009.

[17] B. Cessac, D. Matzakou-Karvouniari, The non linear dynamics of retinal waves, Physica D: Nonlinear Phenomena 439 (2022) 133436.

[18] T. W. Secomb, R. Hsu, E. Y. Park, M. W. Dewhirst, Green's function methods for analysis of oxygen delivery to tissue by microvascular networks, Annals of biomedical engineering 32 (2004) 1519–1529.

[19] A. S. Popel, Theory of oxygen transport to tissue, Critical reviews in biomedical engineering 17 (3) (1989) 257.

[20] D. Goldman, Theoretical models of microvascular oxygen transport to tissue, Microcirculation 15 (8) (2008) 795–811.

[21] T. W. Secomb, A. R. Pries, The microcirculation: physiology at the mesoscale, The Journal of physiology 589 (5) (2011) 1047–1052.

[22] M. Aletti, J.-F. Gerbeau, D. Lombardi, Modeling autoregulation in three-dimensional simulations of retinal hemodynamics, Journal for Modeling in Ophthalmology 1 (2015).

[23] J. Arciero, A. Harris, B. Siesky, A. Amireskandari, V. Gershuny, A. Pickrell, G. Guidoboni, Theoretical analysis of vascular regulatory mechanisms contributing to retinal blood flow autoregulation, Investigative ophthalmology & visual science 54 (8) (2013) 5584–5593.

[24] J. C. Arciero, B. E. Carlson, T. W. Secomb, Theoretical model of metabolic blood flow regulation: roles of atp release by red blood cells and conducted responses, American Journal of Physiology-Heart and Circulatory Physiology 295 (4) (2008) H1562–H1571.

[25] P. Causin, G. Guidoboni, F. Malgaroli, R. Sacco, A. Harris, Blood flow mechanics and oxygen transport and delivery in the retinal microcirculation: multiscale mathematical modeling and numerical simulation, Biomechanics and modeling in mechanobiology 15 (3) (2016) 525–542.

[26] L. Julien, S. Bonnin, M. Paques, J.-M. Fullana, One-dimensional modeling of microvascular hemodynamics in the retina using multimodal imaging, Physics of Fluids 35 (6) (2023).

[27] P. Causin, G. Guidoboni, A. Harris, D. Prada, R. Sacco, S. Terragni, A poroelastic model for the perfusion of the lamina cribrosa in the optic nerve head, Mathematical biosciences 257 (2014) 33–41.

[28] D. Prada, A. Harris, G. Guidoboni, B. Siesky, A. M. Huang, J. Arciero, Autoregulation and neurovascular coupling in the optic nerve head, survey of ophthalmology 61 (2) (2016) 164–186.

[29] Y. Zhu, S. Xu, R. S. Eisenberg, H. Huang, A tridomain model for potassium clearance in optic nerve of necturus, Biophysical journal 120 (15) (2021) 3008–3027.

[30] Y. Mori, A multidomain model for ionic electrodiffusion and osmosis with an application to cortical spreading depression, Physica D: Nonlinear Phenomena 308 (2015) 94–108.

[31] C. S. Henriquez, Simulating the electrical behavior of cardiac tissue using the bidomain model., Critical reviews in biomedical engineering 21 (1) (1993) 1–77.

[32] P. C. Franzone, L. F. Pavarino, S. Scacchi, Mathematical cardiac electrophysiology, Vol. 13, Springer, 2014.

[33] G.-F. Ye, T. W. Moore, D. Jaron, Contributions of oxygen dissociation and convection to the behavior of a compartmental oxygen transport model, Microvascular research 46 (1) (1993) 1–18.

[34] J. M. Olver, D. Spalton, A. McCartney, Quantitative morphology of human retrolaminar optic nerve vasculature., Investigative ophthalmology & visual science 35 (11) (1994) 3858–3866.

[35] E. Onda, G. A. Cioffi, D. R. Bacon, E. M. van BUSKIRK, Microvasculature of the human optic nerve, American journal of ophthalmology 120 (1) (1995) 92–102.

[36] J. U. Harrer, G. J. Parker, H. A. Haroon, D. L. Buckley, K. Embelton, C. Roberts, D. Balériaux, A. Jackson, Comparative study of methods for determining vascular permeability and blood volume in human gliomas, Journal of Magnetic Resonance Imaging: An Official Journal of the International Society for Magnetic Resonance in Medicine 20 (5) (2004) 748–757.

[37] P. Bentzer, L. Kongstad, P.-O. Grände, Capillary filtration coefficient is independent of number of perfused capillaries in cat skeletal muscle, American Journal of Physiology-Heart and Circulatory Physiology 280 (6) (2001) H2697–H2706.

[38] A. Taylor, Capillary fluid filtration. starling forces and lymph flow., Circulation research 49 (3) (1981) 557–575.

[39] R. J. Antcliff, A. A. Hussain, J. Marshall, Hydraulic conductivity of fixed retinal tissue after sequential excimer laser ablation: barriers limiting fluid distribution and implications for cystoid macular edema, Archives of Ophthalmology 119 (4) (2001) 539–544.

[40] D. Camasão, D. Mantovani, The mechanical characterization of blood vessels and their substitutes in the continuous quest for physiological-relevant performances. a critical review, Materials Today Bio 10 (2021) 100106.

[41] M. A. Bartolo, M. U. Qureshi, M. J. Colebank, N. C. Chesler, M. S. Olufsen, Numerical predictions of shear stress and cyclic stretch in pulmonary hypertension due to left heart failure, Biomechanics and modeling in mechanobiology 21 (1) (2022) 363–381.

[42] R. M. Berne, M. N. Levy, B. M. Koeppen, Berne & levy physiology, Elsevier Brasil, 2008.

[43] T. Nagaoka, A. Yoshida, Noninvasive evaluation of wall shear stress on retinal microcirculation in humans, Investigative ophthalmology & visual science 47 (3) (2006) 1113–1119.

[44] M. U. Qureshi, G. D. Vaughan, C. Sainsbury, M. Johnson, C. S. Peskin, M. S. Olufsen, N. Hill, Numerical simulation of blood flow and pressure drop in the pulmonary arterial and venous circulation, Biomechanics and modeling in mechanobiology 13 (5) (2014) 1137–1154.

[45] M. A. Kenfack, F. Lador, M. Licker, C. Moia, E. Tam, C. Capelli, D. Morel, G. Ferretti, Cardiac output by modelflow® method from intra-arterial and fingertip pulse pressure profiles, Clinical science 106 (4) (2004) 365–369.

[46] J. P. Lekakis, N. A. Zakopoulos, A. D. Protogerou, T. G. Papaioannou, V. T. Kotsis, V. C. Pitiriga, M. D. Tsitsirikos, K. S. Stamatelopoulos, C. M. Papamichael, M. E. Mavrikakis, Arterial stiffness assessed by pulse wave analysis in essential hypertension: relation to 24-h blood pressure profile, International journal of cardiology 102 (3) (2005) 391–395.

[47] P. DeSaix, G. J. Betts, E. Johnson, J. E. Johnson, K. Oksana, D. H. Kruse, B. Poe, J. A. Wise, K. A. Young, Anatomy & physiology (openstax) (2013).

[48] N. Safaeian, M. Sellier, T. David, A computational model of hemodynamic parameters in cortical capillary networks, Journal of theoretical biology 271 (1) (2011) 145–156.

[49] E. Roux, P. Bougaran, P. Dufourcq, T. Couffinhal, Fluid shear stress sensing by the endothelial layer, Frontiers in Physiology 11 (2020) 861.

COI

The authors declare that there is no conflict of interest.

Highlights

1. A multi-domain model with vasculature is developed for optic nerve microcirculation.

2. The model includes various physical mechanisms for blood flow and oxygen transport.

3. The vasculature distribution has significant impact on local blood and oxygen supply.

4. Pulsatile arterial pressure produces similar averaged quantity as constant pressure.

5. Effects of the leak across blood vessel wall and other parameters are investigated.

author statement

Zilong Song: Methodology, Formal analysis, Writing- Original draft preparation

Shixin Xu: Methodology, Writing - Review & Editing

Robert Eisenberg: Conceptualization, Methodology, Writing - Review & Editing

Huaxiong Huang: Conceptualization, Methodology, Writing - Review & Editing

Declaration of interests

☒ The authors declare that they have no known competing financial interests or personal relationships that could have appeared to influence the work reported in this paper.

☐ The authors declare the following financial interests/personal relationships which may be considered as potential competing interests: